

Supporting information for

Revisiting cobaloxime(II) chemistry and clearing misconceptions of cobaloxime(II) in
diamagnetic Ni(II) and Pd(II) matrix by comprehensive magnetic measurements

Yukina Suzuki^{1*}, *Mirosław Arczyński*^{1,2}, *Wakizaka Masanori*³, *Hisaaki Tanaka*², *Ryuta Ishikawa*⁴,
Takefumi Yoshida^{5,6}, *Takeshi Yamane*⁷, *Kazunobu Sato*⁷, *Ryota Sakamoto*¹, and *Yamashita*
Masanori^{8,1*}

¹Department of Chemistry, Graduate School of Science, Tohoku University, 6-3 Aramaki-Aza-
Aoba, Aoba-Ku, Sendai 980-8578, Japan

²Faculty of Chemistry, Jagiellonian University, Gronostajowa 2, 30-387 Kraków, Poland

³Department of Applied Chemistry and Bioscience, Faculty of Science and Technology, Chitose
Institute of Science and Technology, 758-65 Bibi, Chitose 066-8655, Japan

⁴Department of Chemistry, Faculty of Science, Fukuoka University, Nanakuma 8-19-1, Fukuoka
814-0180, Japan

⁵Cluster of Nanomaterials, Graduate School of Systems Engineering, Wakayama University, 930
Sakae-Dani, Wakayama, Japan

⁶Physical and Chemical Research Infrastructure Group, RIKEN SPring-8 Center, RIKEN.

⁷Department of Chemistry, Graduate School of Science, Osaka Metropolitan University, 3-3-138
Sugimoto, Sumiyoshi-Ku, Osaka 558-8585, Japan

⁸School of Chemical Science and Engineering, Tongji University, Siping Road 1239, Shanghai
200092, P. R. China

Table of Contents

Experimental	3
Materials and synthetic procedures	3
Synthesis and purity issue of $\text{Co}(\text{Hdmg})_2$	4
Measurements	7
Determination of doping percentage	7
PXRD	8
5% Co(II) in $\text{Ni}(\text{Hdmg})_2$	8
PXRD of 11% Co(II) in $\text{Pd}(\text{Hdmg})_2$	10
EPR spectroscopy	12
Temperature dependence for 5% Co@Ni	12
Temperature dependence for 5% Co@Ni	13
Temperature dependence for 2% Co@Ni	14
Temperature dependence for 11% Co@Pd	15
Comparison between the 5% Co@Ni and 11% Co@Pd.....	16
Simulation of Co@Pd with superhyperfine coupling.....	17
EPR spectra of the exchange-coupled dimers	18
Theoretical calculation	21
Method.....	21
DC magnetic experiments	25
Magnetization of 11% Co@Pd.....	25
Magnetization of 5% Co(II) in $\text{Pd}(\text{Hdmg})_2$	26
The pure $\text{Co}(\text{Hdmg})_2$ experiment	27
PXRD	28
EPR spectroscopy	29
Magnetic measurements	30
$\text{Co}(\text{Hdmg})_2 \cdot 2\text{MeOH}$	31
$\text{Co}(\text{Hdmg})_2 \cdot 2\text{MeOH}$ after solvent removal.....	32
AC susceptibility	32
Oxygen exclusion and magnetic measurements.....	34
Simulation of magnetic data	35
Simulation of susceptibility with different ratios of exchange coupled dimers and $S = 1/2$	35
AC susceptibility	36
5% Co@Ni	36
5% Co@Pd	38

11%Co in Pd(Hdmg) ₂	39
Field dependence of relaxation times of 5% CoNi and 5% CoPd.....	40
Spin-glass experiment.....	41
XANES spectroscopy.....	47
Energy level diagram of clock transitions	48
Co(Hdmg)₂ synthesis and air oxidation	48
IR Spectroscopy	50
References.....	50

Experimental

Materials and synthetic procedures

Co(OAc)₂, Co(OAc)₂•4H₂O, Pd(OAc)₂, dimethylglyoxime, MeOH, EtOH were purchased from Fujifilm Wako Pure Chemical Industries. Ni(OAc)₂•4H₂O was purchased from Sigma Aldrich.

• 5% Co@Ni

Ni(OAc)₂•4H₂O (2.5mmol) and Co(OAc)₂ (2.5mmol) were dissolved in 40 mL MeOH, which was purged with N₂ for 30 min prior to the addition of the salts. To the solution was added dimethyl glyoxime (10 mmol) under the flow of N₂. The solution turned red with immediate precipitations as the ligand was added and the mixture was stirred at room temperature under N₂ for 1 hour. The red solid was collected by filtration under air and washed with copious amounts of MeOH until the filtrate became colorless. To ensure thorough washing, some of the batches were sonicated with MeOH and washed with MeOH. The solids were dried under a vacuum overnight. The doped amount of Co was determined to be about 5% by ICP-AES and XRF(X-ray fluorescence) measurement (Table S1). Elemental analysis Found (%): C 33.51, N 4.99, H 19.13; Calc. (%) C 33.26, N 4.88, H 19.39 (for C₈H₁₄N₄Ni_{0.95}Co_{0.05}O₄)

• 11% Co@Pd

The synthesis was carried out similarly with Co(II) doped Ni(Hdmg)₂. Pd(OAc)₂ and EtOH were used in replace of Ni(OAc)₂•4H₂O and MeOH. The addition of triethylamine to facilitate deprotonation of the glyoxime ligand increases the Co(II) doping percentage up to 11%. Elemental analysis: Found (%) C: 28.70 H: 4.25 N: 16.68, Calc (%): C: 28.95 H: 4.25 N:16.88 (for C₈H₁₄N₄Pd_{0.9}Co_{0.1}O₄)

• Co(Hdmg)₂•2MeOH/EtOH

The synthetic procedure was based on the previous report ¹ with minor modifications. Co(OAc)₂ and the dimethylglyoxime ligand (2 eq) were mixed in MeOH or EtOH in an Ar glove box. The mixture was stirred for 1h and the orangish brown precipitate was collected by vacuum filtration. The solid was washed with the solvent used in the synthesis (MeOH or EtOH) a few times and dried under the Ar atmosphere. The elemental analysis result is found in .

- **Co(Hdmg)₂**

Co(Hdmg)₂•2MeOH/EtOH synthesized as described above was dried under vacuum at 80 °C overnight, following Schrawzer's procedure¹. The elemental analysis result is found in .

Synthesis and purity issue of Co(Hdmg)₂

This section summarizes the synthesis of Co(Hdmg)₂ in the Ni/Pd matrix, the associated purity challenges, and insights from pure Co(Hdmg)₂ studies that rationalize the observed issues. As described in the main text, we were initially expecting to get planar Co(Hdmg)₂ homogeneously dispersed in Ni/Pd(Hdmg)₂. However, EPR spectroscopy and magnetic measurements revealed that our prepared sample contains at least three species, contrary to our expectations. Moreover, the μ -O bridged dimeric species (2) and (3) were found to be dominant over planar Co(Hdmg)₂ (1). This is attributed to the ease of forming axial coordination for Co(Hdmg)₂. Moreover, Ni(Hdmg)₂ was reported to form a dimeric phase analogous to species (2) and (3) in addition to the 1D chain-like crystal structure phase predominantly reported in the literature. The ease of formation and presence of dimeric Co(II) species like (2) may have induced the formation of the dimer phase of Ni(Hdmg)₂, resulting in the heterometallic Ni-Co dimer (3).

The synthesis of Co@Ni and Co@Pd was carried out under an inert atmosphere, following the previous literature that prepared Co(Hdmg)₂ in Ni(Hdmg)₂². Exclusion of air was essential for successfully doping Co(II) into the Ni and Pd matrices, as synthesis conducted in air yielded diamagnetic products. This outcome is attributed to the high sensitivity of Co(Hdmg)₂ to axial coordination by molecular oxygen. The strong affinity of square planar Co(II) complexes for O₂ has been extensively studied due to its biological importance³⁻⁷.

The purity of the synthesized Co@Ni/Pd was initially assessed using powder X-ray diffraction (PXRD) prior to conducting any magnetic measurements (Figure S1-Figure S4). The doped samples exhibited PXRD patterns identical to those of pristine Ni/Pd(Hdmg)₂, leading to the initial assumption that Co(II) was homogeneously incorporated into the Ni/Pd matrix while preserving the original Ni/Pd(Hdmg)₂ crystal structure. However, EPR spectroscopy and magnetic measurements, as later discussed, revealed that the doped Co(II) was highly defective, existing as multiple Co(II) species (1) - (3) and not uniformly distributed in the diamagnetic Ni/Pd(Hdmg)₂ matrix, contradicting our initial assumption.

The existence of multiple Co(II) species, as identified by EPR spectroscopy, initially confused us because no signs of impurity were detected in the PXRD patterns. To gain further insight, we conducted additional macroscopic analytical techniques, but these also failed to provide information about Co(II) impurities. In retrospect, this is unsurprising; elemental analysis cannot distinguish polymorphic forms or defective dimeric Co(II) species (2) and (3), as these variations do not alter the overall composition. Similarly, FT-IR spectroscopy (Figure S42) primarily reflected the bulk properties of the host matrix, offering no specific information on the Co(II) species.

Faced with this purity issue, we attempted to synthesize the pristine Co(II)(Hdmg)₂ to better understand its properties. The oldest account of the synthesis of Co(Hdmg)₂ was published by

Schrauzer in 1966¹. By that time, a wide range of $[\text{Co}(\text{Hdmg})_2\text{B}_2]$ complexes (where B represents a Lewis base ligand, typically a coordinating solvent molecule) were already known. However, the preparation of pristine $\text{Co}(\text{Hdmg})_2$ proved significantly more challenging, with Schrauzer referring to it as a “long-sought compound.” This difficulty stems from the strong propensity of planar $\text{Co}(\text{Hdmg})_2$ to form axial coordination. Reactions between $\text{Co}(\text{II})$ salts and glyoxime ligands in polar solvents such as MeOH, H_2O , or EtOH typically yield solvent-coordinated $\text{Co}(\text{Hdmg})_2$ species, where the axial positions are occupied by solvent molecules¹. The strong tendency for axial coordination is also suggested by the existence of dimers/polymers of $\text{Co}(\text{Hdmg})_2$ ^{8–11}.

Schrauzer’s synthesis was later adopted by other researchers to investigate the electronic structure of planar $\text{Co}(\text{Hdmg})_2$, primarily by EPR spectroscopy¹². In many of these studies, $\text{Co}(\text{Hdmg})_2$ was dissolved in various solvents, such as alcoholic solutions, pyridine, and THF/toluene. EPR measurements revealed smaller g-factors for $\text{Co}(\text{Hdmg})_2$ in these solvents compared to those observed in the $\text{Ni}(\text{Hdmg})_2$ host, which exhibited the largest g-factor (g_x) of 2.57. The EPR data for $\text{Co}(\text{Hdmg})_2$ in the $\text{Ni}(\text{Hdmg})_2$ host was regarded as an extreme case of negligibly weak axial interactions. Deviations in EPR parameters from those observed in the $\text{Ni}(\text{Hdmg})_2$ host were subsequently used as a metric to evaluate the extent of axial coordination in other environments. However, as we have demonstrated, the true planar $\text{Co}(\text{Hdmg})_2$ with extremely weak axial interaction results in a g factor as large as 4.75 in species (**1**).

Schrauzer’s original procedure¹ mixed $\text{Co}(\text{II})$ acetate tetrahydrate with the glyoxime ligand in MeOH to obtain $[\text{Co}(\text{Hdmg})_2\text{B}_2]$ complex ($\text{B} = \text{H}_2\text{O}$). This compound was then evacuated at elevated temperatures to remove the coordinating solvent molecules, as described in the original literature. Elemental analysis of the vacuum-dried species confirmed the removal of solvents, with the chemical composition matching $\text{Co}(\text{Hdmg})_2$. Identical procedure but starting from anhydrous $\text{Co}(\text{II})$ acetate in MeOH or EtOH led $[\text{Co}(\text{Hdmg})_2\text{B}_2]$ complex ($\text{B} = \text{MeOH}$ or EtOH) with relatively good crystallinity (see the pure $\text{Co}(\text{Hdmg})_2$ experiment section in the SI). The subsequent evacuation yielded solvent-removed species, as confirmed by elemental analysis (Refer to the pure $\text{Co}(\text{Hdmg})_2$ experimental section). Unfortunately, solvent removal results in a significant loss of crystallinity, making it difficult to study the structural and magnetic properties of $\text{Co}(\text{Hdmg})_2$ in detail. To this date, the single crystal structure of $\text{Co}(\text{Hdmg})_2$ is not known. For the same reason, PXRD cannot be used in our study to verify the purity of doped samples obtained in a similar manner; The lack of obvious signs of impurities by PXRD can also be explained by the amorphous nature of pristine $\text{Co}(\text{Hdmg})_2$. Obtaining crystalline $\text{Co}(\text{Hdmg})_2$ without solvent molecules by recrystallization is also not possible as this $\text{Co}(\text{Hdmg})_2$ is practically insoluble in all inert nonpolar solvents as Schrauzer described.

Magnetic studies conducted on the pristine $\text{Co}(\text{Hdmg})_2$ prepared as described suggested that the majority of the $\text{Co}(\text{II})$ complexes formed antiferromagnetically coupled dimers (See the pure $\text{Co}(\text{Hdmg})_2$ experimental section). Though the specific geometry of the dimerized $\text{Co}(\text{Hdmg})_2$ could not be conclusively determined due to the poor crystallinity of the evacuated sample, the formation of a dimer, likely $[\text{Co}(\text{Hdmg})(\mu\text{-Hdmg})]_2$, is consistent with the strong

tendency of $\text{Co}(\text{Hdmg})_2$ to form axial coordination. The DC magnetic measurement revealed a very similar antiferromagnetic exchange coupling interaction with $[\text{Co}(\text{salen})]_2$ ($\text{salen} = N,N'$ -bis(salicylaldehyde)ethylenediimine) whose structure is analogous to $[\text{Co}(\text{Hdmg})(\mu\text{-Hdmg})]_2$. The magnitude of antiferromagnetic interaction found in the pure sample ($J = -21.8\text{cm}^{-1}$) was remarkably similar to that of dimeric $\text{Co}(\text{salen})$ ($J = -21\text{cm}^{-1}$)^{13,14}, which was already noted from the similarity of EPR spectra². This further supports the $[\text{Co}(\text{Hdmg})(\mu\text{-Hdmg})]_2$ dimer formation upon solvent removal.

In addition, the magnetic measurements suggest a few other impurities like $S = 1/2$ monomeric species, likely due to the highly defective and amorphous nature of the evacuated product. Though the pure crystalline $\text{Co}(\text{Hdmg})_2$ could not be obtained, these results clearly indicate that preparing $\text{Co}(\text{Hdmg})_2$ is significantly challenging and the dimeric phases like $[\text{Co}(\text{Hdmg})(\mu\text{-Hdmg})]_2$ are always favored over planar $\text{Co}(\text{Hdmg})_2$.

Based on the pure $\text{Co}(\text{Hdmg})_2$ synthesis and magnetic data, the formation of species **(2)** and **(3)** in $\text{Ni/Pd}(\text{Hdmg})_2$ can be rationalized as follows. First, as already stated, the strong tendency to form axial coordination justifies the presence of dimeric species **(2)** and **(3)**. Furthermore, a dimeric phase of $\text{Ni}(\text{Hdmg})_2$ will explain the presence of the bimetallic dimer **(3)**. The crystal structure of $\text{Ni}(\text{Hdmg})_2$, though is predominantly reported as a pseudo-1D chain structure as in Figure 1 (Space group: *Ibam*), another phase has also been observed, characterized by $\mu\text{-O}$ bridges through the oxime oxygen (Space group: $P2_1/c$)¹⁵ (Figure 3). This $P2_1/c$ crystal was prepared by refluxing $\text{Ni}(\text{Hdmg})_2$ in DMF and then slowly cooling the filtrate solution. In contrast, bulk $\text{Ni}(\text{Hdmg})_2$ prepared by fast precipitation, only exhibits the *Ibam* phase, suggesting that this is the kinetically favored product. The $P2_1/c$ phase, which required a slow crystallization process at an elevated temperature, may therefore represent the thermodynamically favored form. In the synthesis of $\text{Ni/Pd}(\text{Hdmg})_2$, the fast preparation of the compound leads to the sample precipitating as only the *Ibam* phase. However, the presence of $\text{Co}(\text{Hdmg})_2$ that tends to dimerize, as shown by the pristine experiment and other literature^{8,9,16}, in the reaction mixture to produce $\text{Co}(\text{II})$ doped $\text{Ni/Pd}(\text{Hdmg})_2$ might shift the equilibrium of different phases, inducing some of $\text{Ni}(\text{Hdmg})_2$ to the second $P2_1/c$ dimer phase. This induction of the $P2_1/c$ phase of $\text{Ni}(\text{Hdmg})_2$ by the presence of $\text{Co}(\text{II})$ complexes can be inferred from the existence of bimetallic dimer species **(3)** in addition to homometallic Co dimers **(2)**. The lack of diffractions by this phase in PXRD might be due to that these dimer species **(2)** and **(3)** are occluded in the 1D chain of $\text{Ni}(\text{Hdmg})_2$ in a highly defective manner.

Given the reasons and the properties of $\text{Co}(\text{Hdmg})_2$ mentioned above, preparing a homogeneous $\text{Co}(\text{Hdmg})_2$ in $\text{Ni/Pd}(\text{Hdmg})_2$ has been unsuccessful. The persistent precipitation of the three $\text{Co}(\text{II})$ species **(1)**-**(3)** suggests that the existence of multiple phases is due to the intrinsic nature of $\text{Co}(\text{Hdmg})_2$ rather than a simple impurity issue. We therefore proceeded to analyze this inhomogeneous material, as presented in the main text.

Measurements

The elemental analysis was carried out by J-Science Lab Co. Ltd. JM11 at the Research and Analytical Center for Giant Molecules (Tohoku Univ.). ICP-OES was measured by SPECTRO ARCOS at the Institute of Multidisciplinary Research for Advanced Materials (Tohoku Univ.). XRF (X-ray Fluorescence) spectroscopy was measured by Rigaku Supermini200 at the Research Institute of Electrical Communication (Tohoku Univ.) or Rigaku NEX-DE. PXRD measurements were carried out with Cu K α radiation using a Rigaku Ultima IV diffractometer at room temperature. Magnetic measurements were performed using a magnetic property measurement system (MPMS-XL, Quantum Design) and a physical property measurement system (PPMS-6000, Quantum Design). For magnetic measurements, the solid sample was filled into a gelatin capsule (Matsuya) and attached to a plastic straw with Kapton tape. Room temperature EPR spectra were measured with X330 (JEOL) at the Department of Applied Chemistry, Chemical Engineering, and Biomolecular Engineering (Tohoku Univ.). ESR spectra at low temperatures were measured at X-band using a Bruker E-500 spectrometer equipped with a gas-flow type cryostat Oxford ESR 900. The simulation of the ESR spectra was performed on EasySpin. The X-ray absorption fine structure (XAFS) measurements of the pellet of powder samples at RT were carried out at the BL36XU beamline on SPring-8¹⁷. Analysis was performed using the Demeter software platform¹⁸.

Determination of doping percentage

The amount of Co doped in the diamagnetic matrices was determined by either/both XRF or/and ICP-OES. Table S1 shows the percentage of Co in the representative samples (5% Co@Ni and 11% Co@Pd) using different measurements or equipment. XRF and ICP-OES gave quite close results for the 5% Co in Ni(Hdmg)₂ case. Different XRF apparatus also gave similar results for 11% Co in Pd(Hdmg)₂. Given that those different measurements result in similar Co percentages with differences of less than 1%, the errors in XRF and ICP-OES measurements are assumed to be small.

Table S1. The Co doping percentage determined by XRF and ICP-OES

	XRF ¹	XRF ²	ICP-OES
5% Co(II) in Ni(Hdmg) ₂	5.0		4.8
11% Co(II) in Pd(Hdmg) ₂	10.8%	10.6%	

1: Rigaku NEX-DE

2: Rigaku Supermini200

PXRD

5% Co(II) in Ni(Hdmg)₂

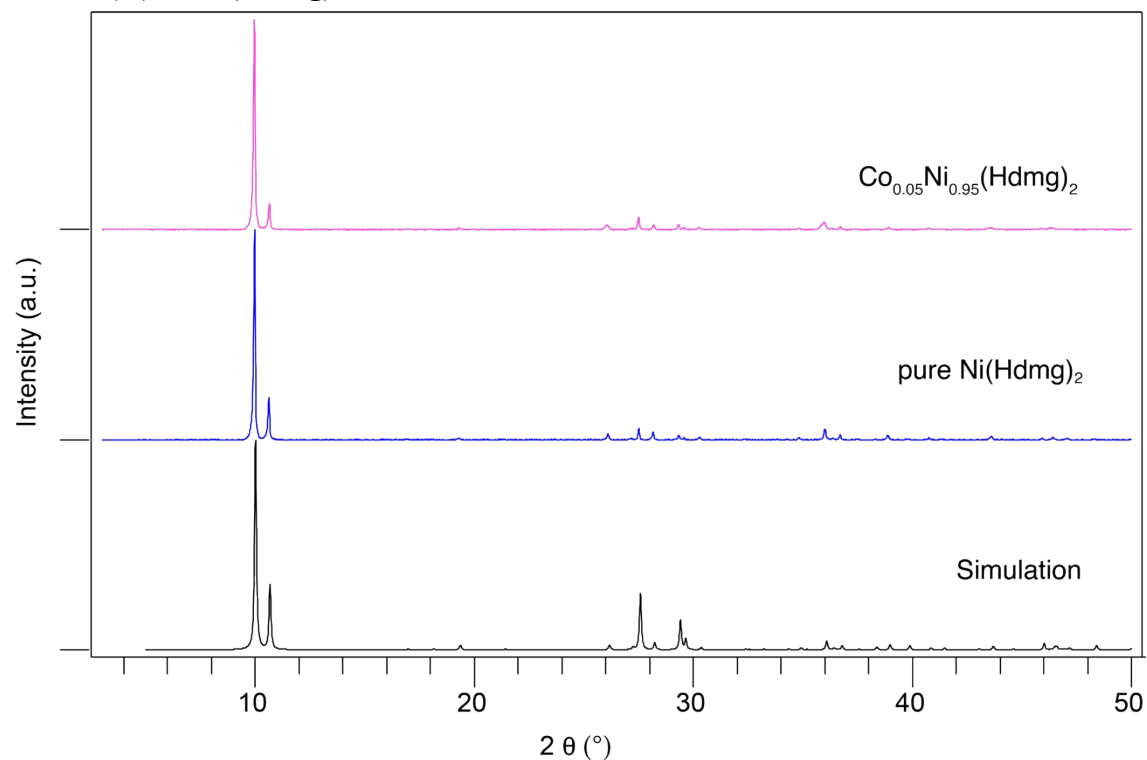


Figure S1. The powder XRD patterns of pure and 5% Co@Ni (pink) with the PXRD pattern of pristine Ni(Hdmg)₂ and simulated pattern from a single crystal structure (black). The peak position of the doped system remains the same as the pure Ni(Hdmg)₂.

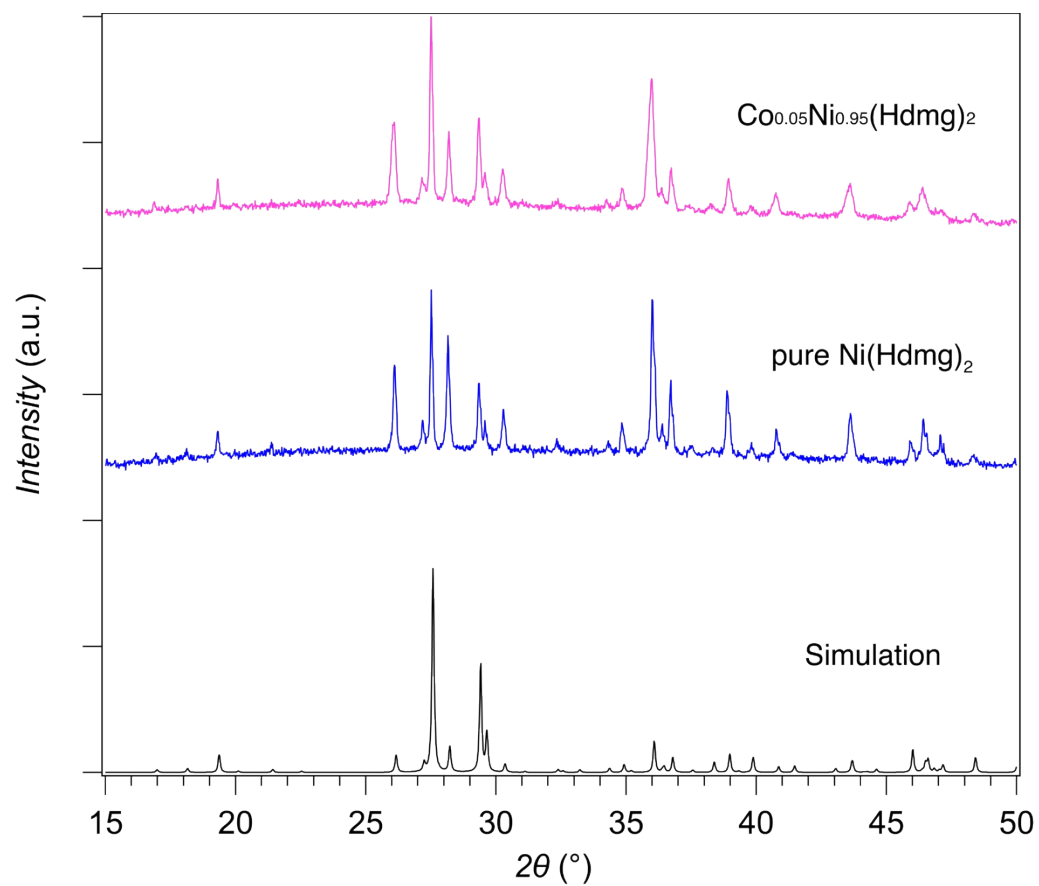


Figure S2. The magnified powder XRD pattern of pure and Co@Ni from $2\theta = 15^\circ$ to 50° . The peak position of the doped system remains the same as the pure Ni(Hdmg)₂.

PXRD of 11% Co(II) in Pd(Hdmg)₂

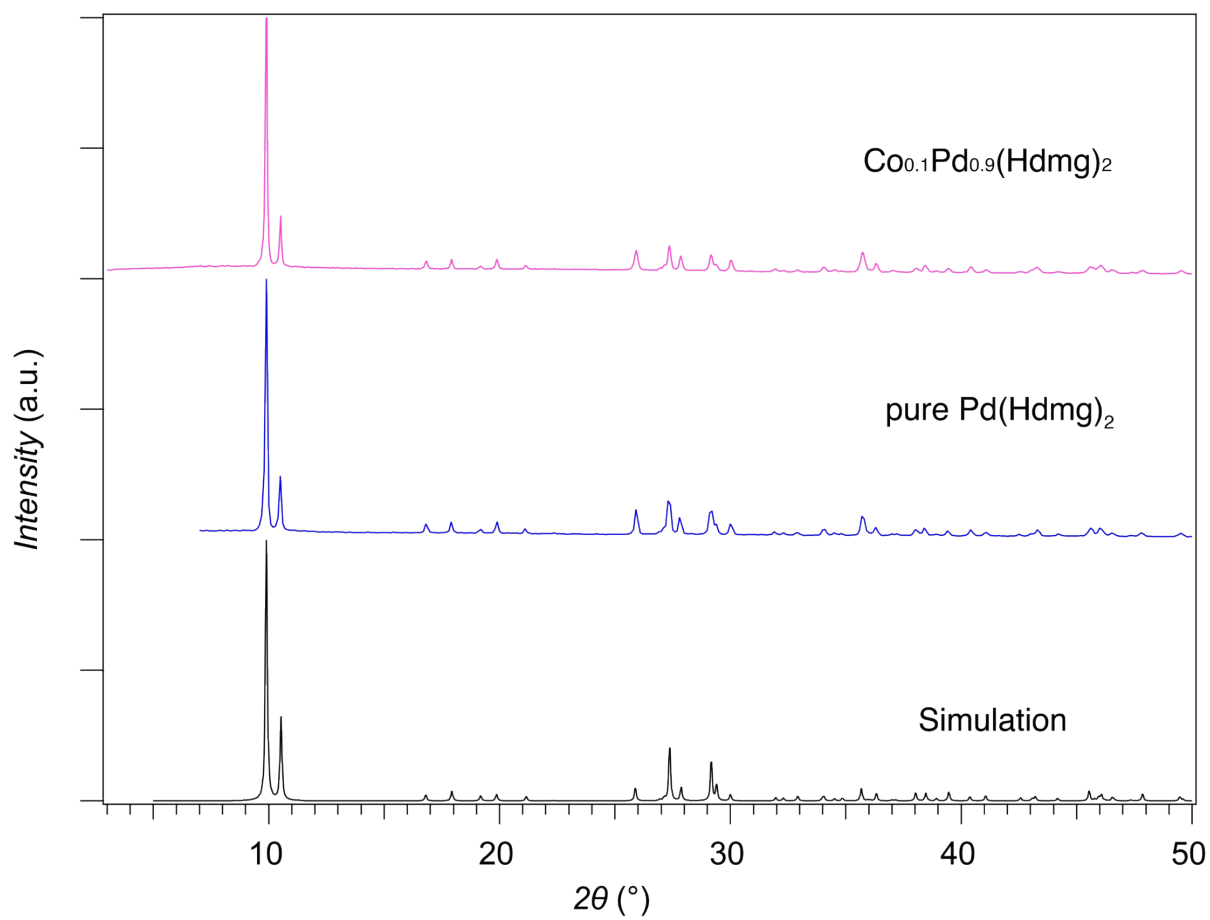


Figure S3. The powder XRD pattern of simulated, synthesized pure $\text{Pd}(\text{Hdmg})_2$, and 11% Co@Pd.

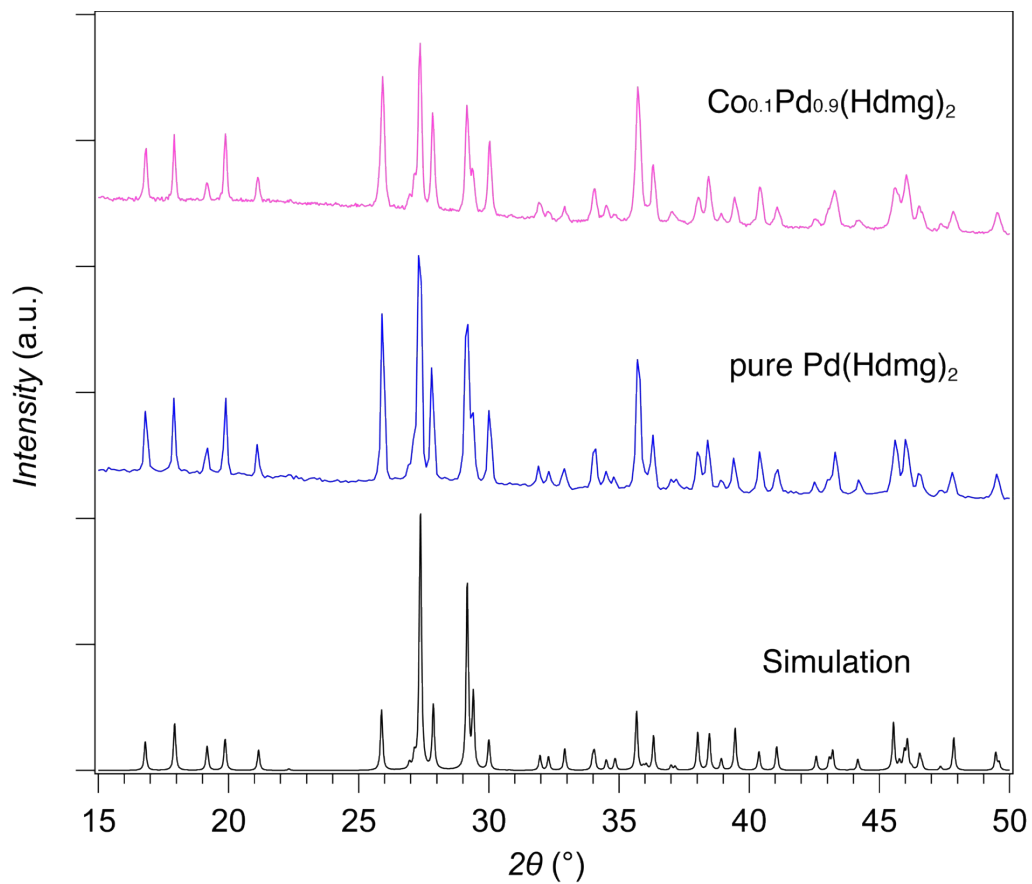


Figure S4. The magnified powder XRD pattern of pure and 11% Co@Pd from $2\theta=15^\circ$ to 50° . The peak position of the doped system remains the same as the pure $\text{Pd}(\text{Hdmg})_2$.

EPR spectroscopy

Temperature dependence for 5% Co@Ni

The initial low-temperature EPR measurement was done by an EPR spectrometer only accessible up to 800 mT.

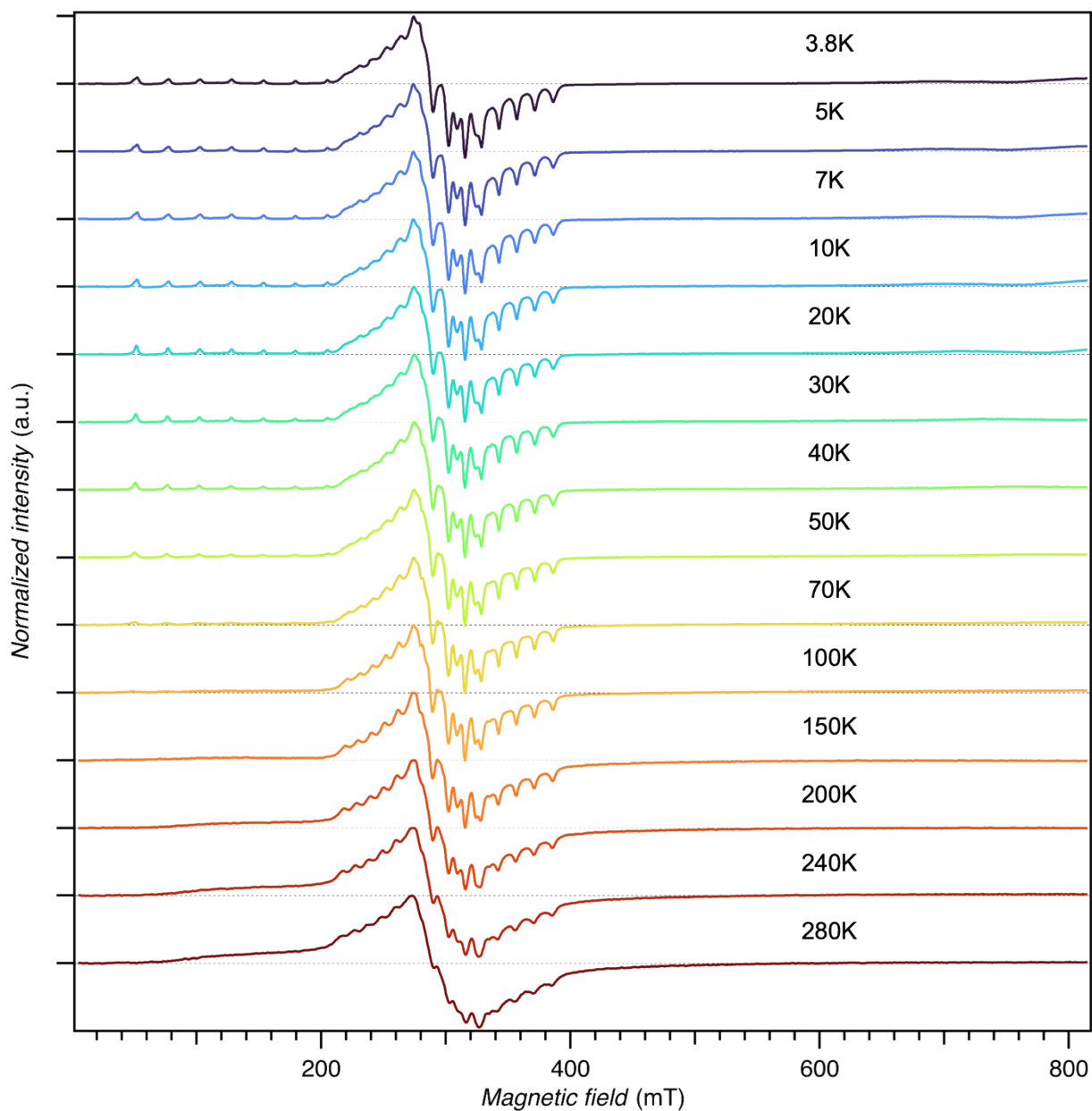


Figure S5. Variable-temperature EPR spectra of 5% Co@Ni

Temperature dependence for 5% Co@Ni

A different spectrometer was used to measure the low-temperature data up to 1100 mT on the same sample. The sharp peaks result from residual molecular oxygen likely not fully removed during EPR sample preparation, as similar peaks are absent in Figure S5.

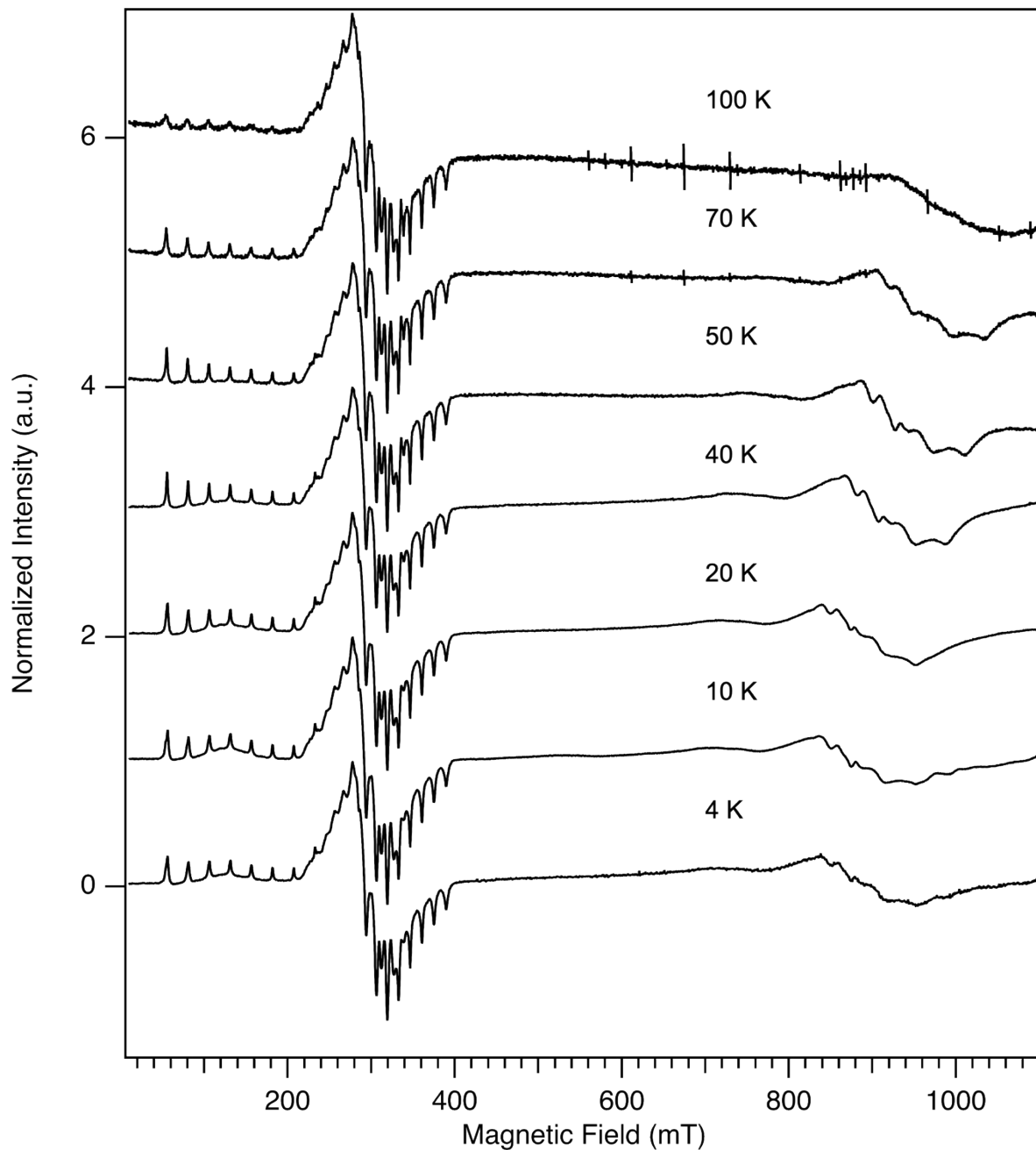


Figure S6. Variable-temperature EPR spectra of 5% Co@Ni.

Temperature dependence for 2% Co@Ni

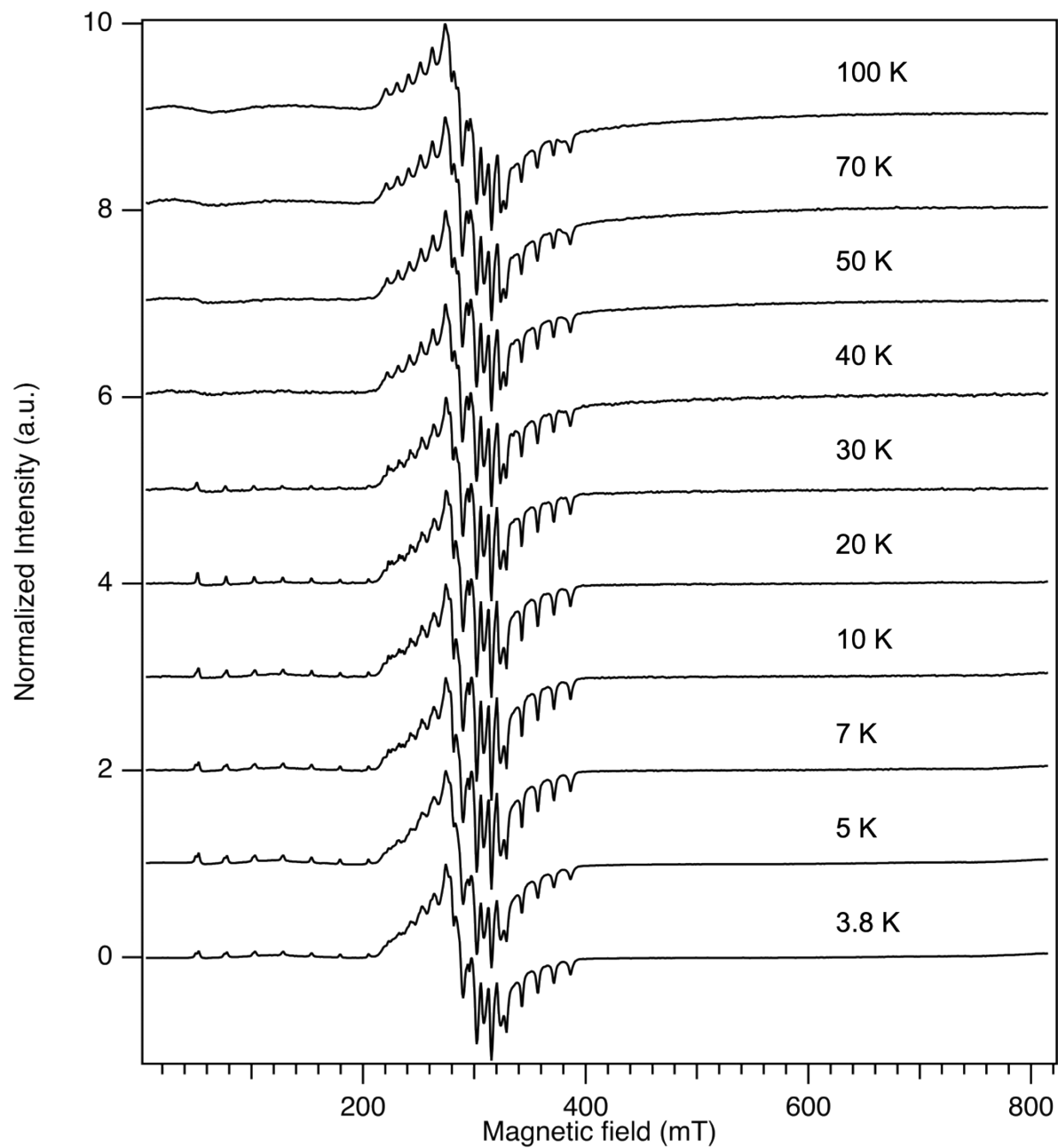


Figure S7. Variable-temperature EPR spectra of 2% Co@Ni.

Temperature dependence for 11% Co@Pd

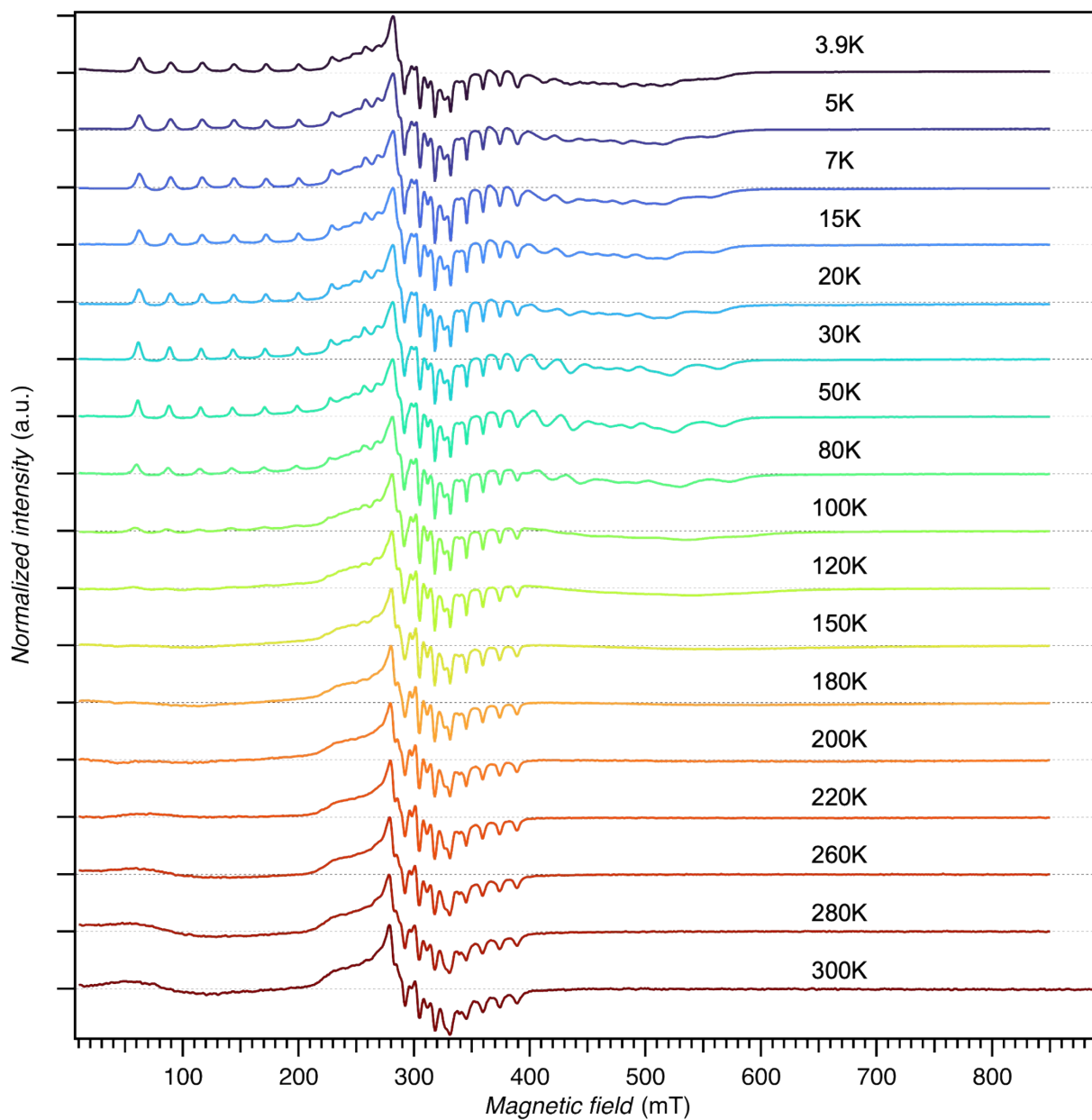


Figure S8. Variable-temperature EPR spectra of 11% Co@Pd

Comparison between the 5% Co@Ni and 11% Co@Pd

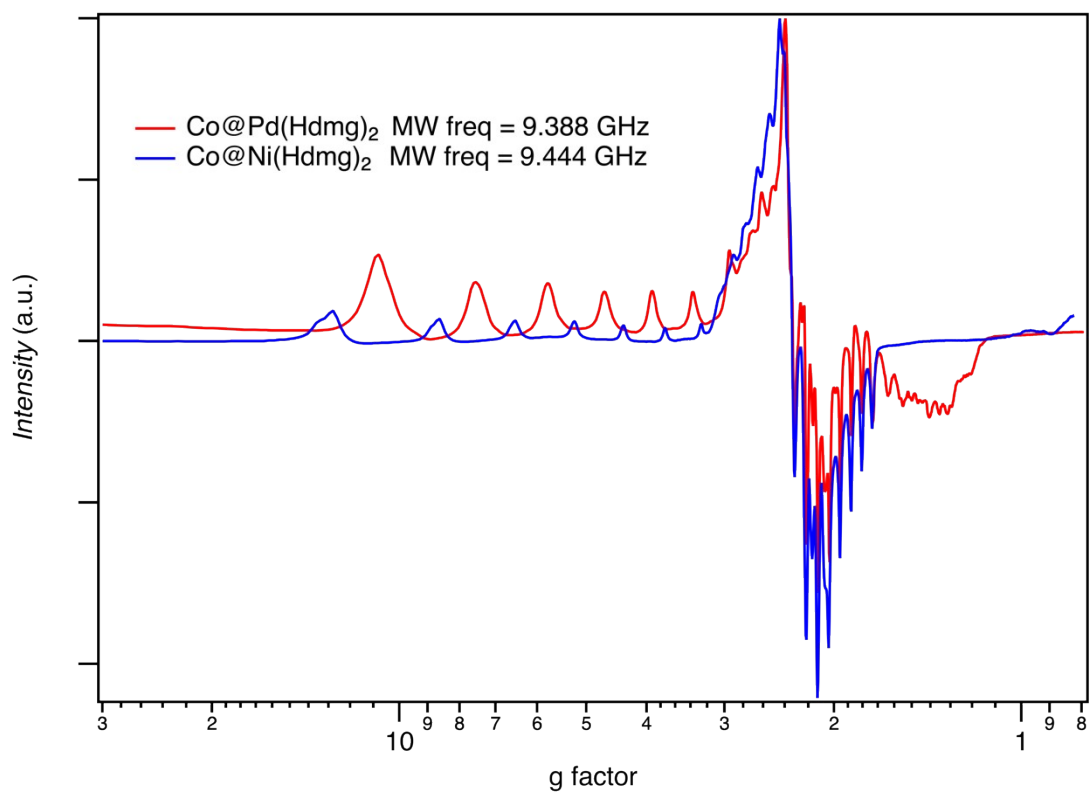


Figure S9. The comparison of the EPR spectra of Co@Ni(blue) and Co@Pd(red).

Simulation of Co@Pd with superhyperfine coupling

Figure S10 shows a simulation of Co@Pd spectra at 3.8 K. The addition of superhyperfine coupling with a ^{105}Pd nuclei of an arbitrary size tabulated in Table S2 reproduced the small peaks at the high field better.

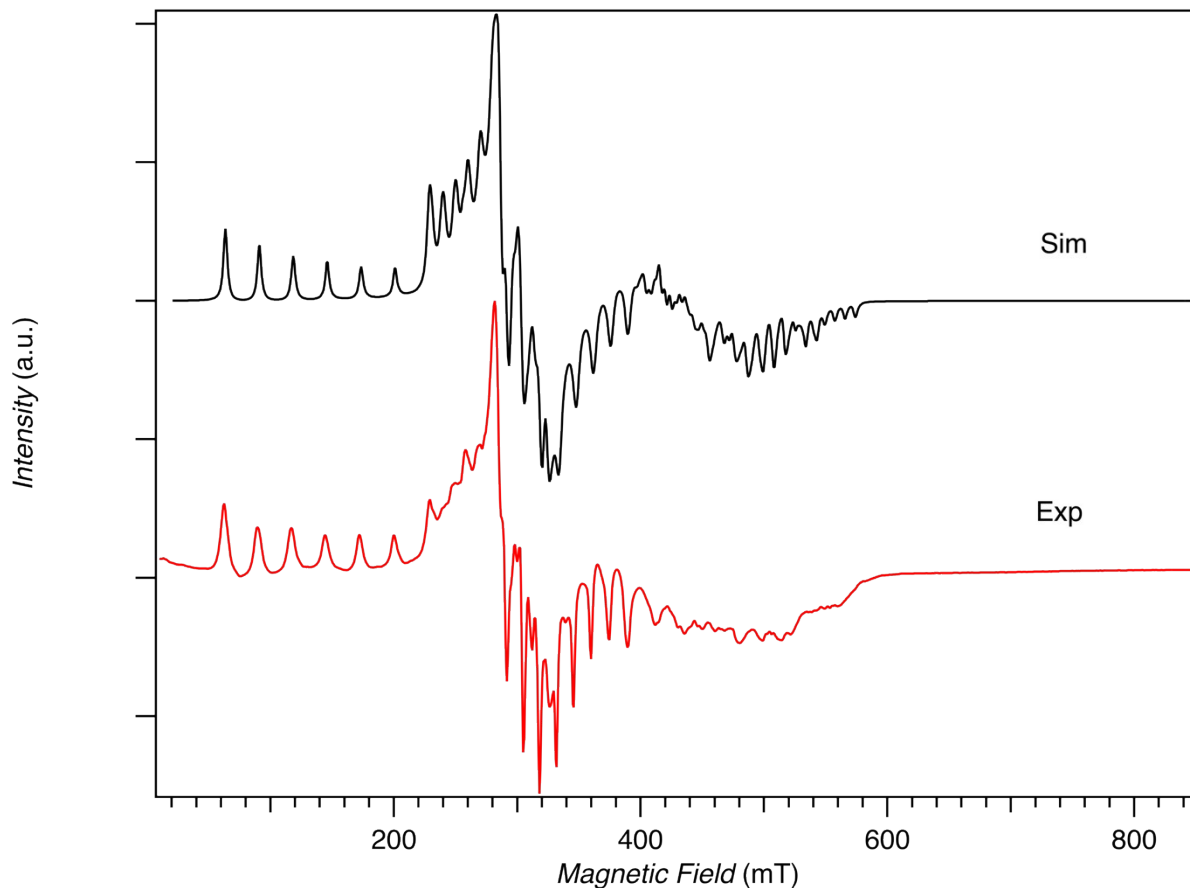


Figure S10. A simulated spectra (black) of Co@Pd including the superhyperfine coupling with ^{105}Pd ($I = 5/2$ 22.33% natural abundance) nuclear spins. The red line is the experimental spectrum.

Table S2. The parameters used for Figure S10.

g_1	g_2	g_3	A_{Co1}	A_{Co2}	A_{Co3}	A_{Pd1}	A_{Pd2}	A_{Pd3}	g strain	Line width (Lorentzian, Gaussian)
4.22	1.66	1.43	1630	157	210	0	100	200	(0, 0.008, 0.002)	(0, 2)

EPR spectra of the exchange-coupled dimers

Although SQUID magnetometry detected antiferromagnetically coupled dimers ($S = 0$) that can be thermally excited into $S = 1$ states, no obvious sign of these species was observed in our EPR spectra. This absence is likely due to the significant spectral broadening of the triplet state and overlaps with the signals from other species.

For exchange-coupled systems, the EPR spectrum is typically characterized by zero-field splitting parameters D and E ¹⁹. Especially when the exchange interaction is much larger than the EPR excitation frequency, as in our case ($|J|=21\text{cm}^{-1} \gg h\nu \sim 0.3 \text{ cm}^{-1}$ at X-band). The observability of EPR transitions depends largely on the magnitude of D . When $D \ll h\nu$, the EPR spectrum often features a “half-field transition” ($g \sim 4$), corresponding to the forbidden $m_s = -1 \rightarrow m_s = 0$ transition at half the field value of the allowed $m_s = -1 \rightarrow m_s = -1$ and $m_s = 0 \rightarrow m_s = +1$ transitions ($g \sim 2$)¹⁹⁻²¹.

Although we lack knowledge of D and E parameters for our dimers, we measured the EPR spectra of the pure $[\text{Co}(\text{salen})]_2$ dimer (Figure S11), an analog of our system that shows a similar size of exchange coupling. Comparing the spectrum of exchange coupled $[\text{Co}(\text{salen})]_2$ to that of $S = 1/2$ $[\text{Co}(\text{salen})\text{Zn}(\text{salen})]$, we observed significant spectral broadening in the spectrum of the dimer. The EPR signal of the $S = 1$ dimer appears at a similar position to that of diluted $S = 1/2$ $\text{Co}(\text{salen})$. The absence of a half-field peak could be attributed to either excessive broadening or the inherently weak nature of this forbidden transition, which has been observed in other systems²². We note that a small, sharp feature in the spectrum may arise from paramagnetic $S = 1/2$ monomeric impurities, which are commonly found in dimeric systems²³, including this compound¹⁴. Our SQUID measurements also confirmed the presence of these $S = 1/2$ impurities.

Based on the EPR spectra of $[\text{Co}(\text{salen})]_2$, the lack of a clear triplet signal likely results from substantial spectral broadening hidden by other spectral features. Assuming that the spectra appear around the same position with $S = 1/2$ heterometallic dimer similar to $[\text{Co}(\text{salen})]_2$, their broad peaks around $g \sim 2$ can be easily masked by the $S = 1/2$ heterometallic dimer signal. This might also explain why the spectra around $g \sim 2$ (RT components) look broader than the similar percentage of 5% $S = 1/2$ $[\text{Co}(\text{salen})\text{Zn}(\text{salen})]$. Furthermore, closer examination of the temperature-dependent EPR spectra (Figure S5) reveals broadening at the edges of peaks around 200 mT and 400 mT. This broadening may be due to $\text{Co}(\text{II})$ in the heterometallic dimers. The previous study of $[\text{Co}(\text{salen})]_2$ showed that thermal energy surpasses the exchange coupling strength, leading to behavior characteristic of $S = 1/2$ spins at higher temperatures ($> 200 \text{ K}$)¹³. While the electronic structure of these thermally activated $S = 1/2$ spins in the homometallic dimers should resemble that of the heterometallic counterpart $[\text{Co}(\text{Hdmg})_2\text{Ni}(\text{Hdmg})_2]$, it is expected that they experience stronger magnetic interactions due to the presence of another $S = 1/2$ spin within the dimer.

Similarly, a close inspection of the $g \sim 4-5$ spectra region (Figure 12, Figure S6) shows there is a broad feature underlying the sharp peaks of $\text{Co}(\text{Hdmg})_2$ at low temperatures. The feature seems to be growing with increasing temperature up to 30 -40 K, where a significant amount of dimers are excited into the triplet state¹³. These broad features are also likely to originate from triplet dimers.

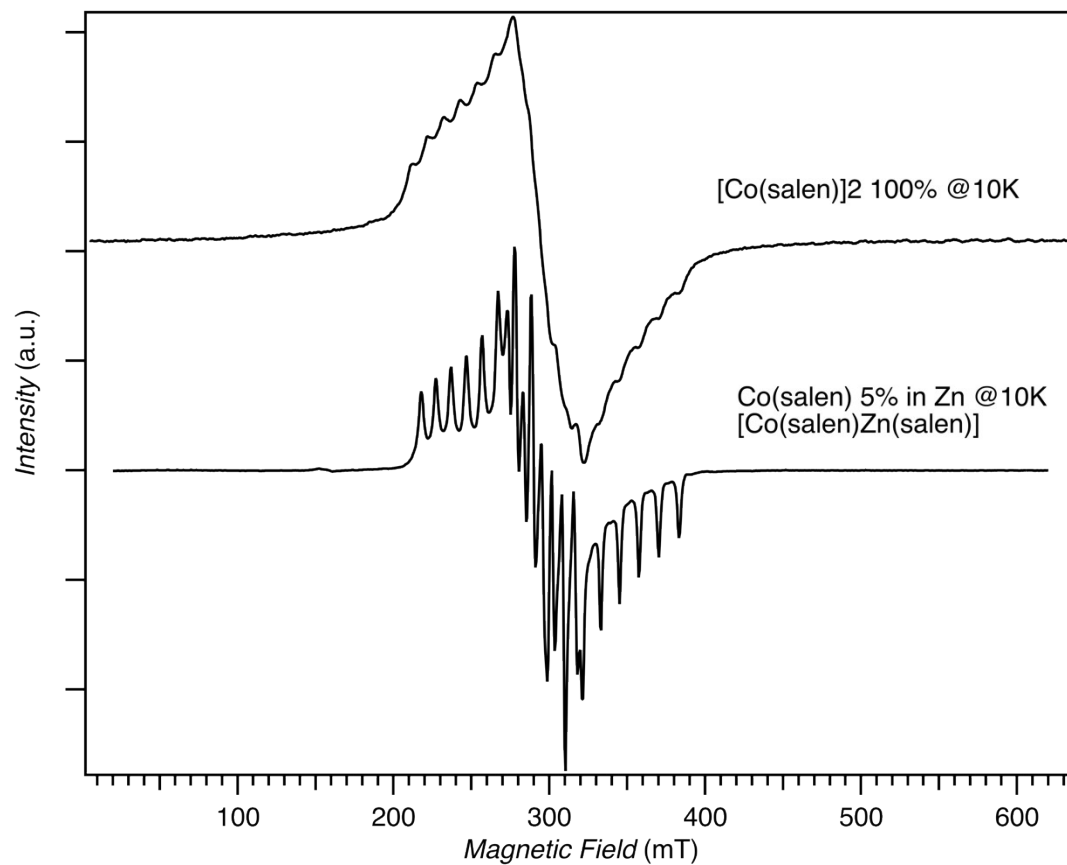


Figure S11 The EPR spectra of 5% dimeric Co(salen) diluted in Zn(salen) ([Co(salen)Zn(salen)]) and pure [Co(salen)]₂ at 10 K

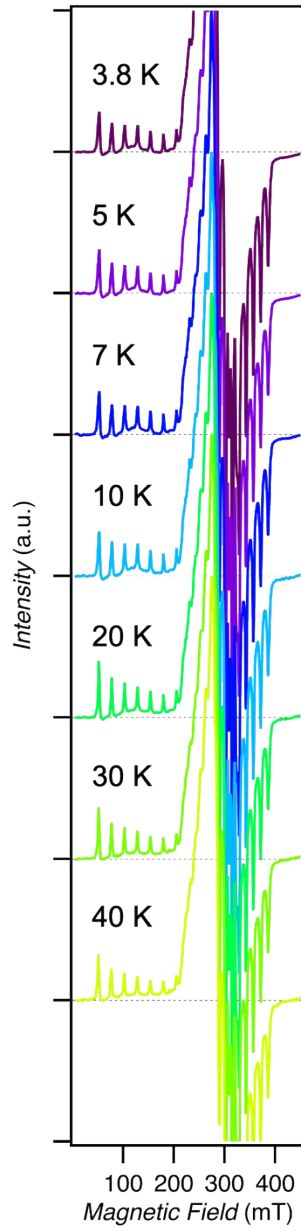


Figure 12. The EPR spectra of 5%Co@Ni at low temperatures at a closer look at the low-field region.

Theoretical calculation

Method

Gas-phase geometries of high-spin and low-spin cobalt(II) complexes [Co(Hdmg)₂] in the ground state were optimized using density functional theory (DFT) level, employing Grimme's B97-D3 pure generalized gradient approximation (GGA) functional^{24,25}. The Co center was treated with the Stuttgart-Cologne ECP10MDF basis set and fully relativistic effective core potential (ECP) combination²⁶. For the C, N, and O atoms of Hdmg⁻ ligands, the Stuttgart-Cologne ECP2MWB basis set and quasi-relativistic effective core potential combination²⁷ were used. For the remaining H atoms, the Dunning-Hay polarized double- ζ quality (DZP) basis^{28,29} with a diffuse function was used. In addition, polarization functions were added to basis sets of Co, C, N, O, and H atoms, obtained from the EMSL basis set exchange website³⁰⁻³². The atoms and their polarization functions were: Co ($\alpha_f = 4.076$, $\alpha_d = 1.019$), C ($\alpha_d = 0.720$), N ($\alpha_d = 0.980$), O ($\alpha_d = 1.280$), and H ($\alpha_d = 1.000$), respectively. Their appropriate methods give reliable geometries and are widely used in many computational studies for metal complexes[14]. For accuracy, the TightSCF and Opt convergence criteria and the ultrafine integration grid for all atoms were used in geometry optimizations. The structural optimizations were performed with the Gaussian 09 Revision D.01 suite of program³³.

The zero-field splitting parameters and *g*-tensors were also performed using *ab initio* state-average complete active space self-consistent field (SA-CASSCF) method followed by second-order N-electron valence perturbation theory (NEVPT2) method, where the atomic coordinate was used in the DFT-optimized structures (vide supra). These calculations were performed using the parallel version of the ORCA 5.0.4. program package^{34,35}. Before the CASSCF method, the DFT approach was performed to get the starting guess orbitals with the spin-unrestricted GGA functional BP86^{36,37} and subsequently the quasi-restricted orbital^{38,39}. Spin-orbit coupling was accounted for by quasi-degenerate perturbation theory formulation^{40,41}. The second-order Douglas-Kroll-Hess (DKH) scalar relativistic Hamiltonian⁴² was used in combination with the DKH-recontracted Ahlrich's all electron polarized triple- ζ quality def2-TZVP⁴³ basis on all atoms. The auxiliary basis set of AutoAux was used to fit electron density in The resolution-of-identity chain-of-spheres exchange approximations⁴⁴. The active space consisted of only the five 3d-orbitals and seven electrons (CAS(7,5)). 10 quartet and 40 doublet roots were included as they are sufficient for high-spin and low-spin Co^{II} centers. The final Spin-Hamiltonian parameters reported here are based on the effective Hamiltonian approach. All calculation processes were set to default.

Table S3. xyz-coordinates for high-spin [Co(Hdmg)₂].

	<i>x</i>	<i>y</i>	<i>z</i>
Co	0.00000	0.00000	0.00000
N	0.48801	-1.16234	-1.53246
N	0.48808	1.16231	1.53246
N	-1.12918	0.79747	-1.41375
N	-1.12922	-0.79742	1.41374
C	-0.97213	0.29030	-2.61949
C	-0.08290	-0.83425	-2.70636

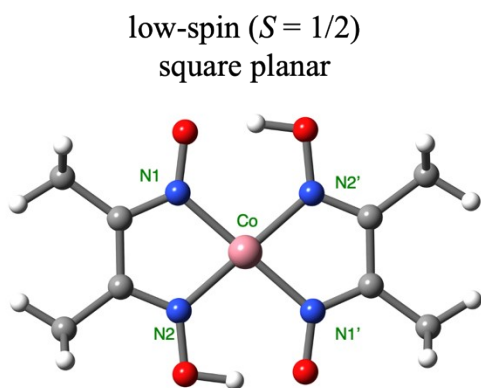
C	-0.97214	-0.29024	2.61948
C	-0.08285	0.83425	2.70636
O	1.26546	2.14210	1.39803
O	1.26534	-2.14218	-1.39803
O	-1.99917	1.88303	-1.35045
O	-1.99927	-1.88293	1.35045
C	0.19695	-1.59303	-3.95755
H	0.92898	-2.37214	-3.73400
H	-0.70433	-2.07179	-4.35986
H	0.60642	-0.94655	-4.74262
C	-1.69189	0.85207	-3.79760
H	-1.43403	1.90888	-3.92512
H	-1.44970	0.31236	-4.71254
H	-2.77454	0.81472	-3.63516
C	0.19705	1.59301	3.95755
H	0.92912	2.37209	3.73400
H	-0.70420	2.07181	4.35987
H	0.60649	0.94650	4.74262
C	-1.69194	-0.85198	3.79760
H	-1.43411	-1.90879	3.92514
H	-1.44974	-0.31227	4.71254
H	-2.77458	-0.81460	3.63515
H	-1.92290	2.16738	-0.43034
H	-1.92302	-2.16728	0.43034

Table S4. *xyz*-coordinates for low-spin [Co(Hdmg)₂]

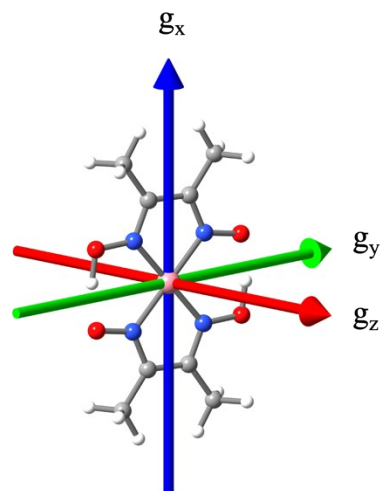
Co	0.00000	0.00000	0.00000
O	1.23782	-2.53480	-0.00054
O	1.28666	2.56095	0.00053
O	-1.23766	2.53486	0.00026
O	-1.28686	-2.56091	-0.00024
N	1.40510	-1.26099	-0.00032
N	1.40610	1.22270	-0.00053
N	-1.40505	1.26106	0.00017
N	-1.40619	-1.22264	0.00062

C	2.63024	-0.73272	-0.00004
C	2.62184	0.70763	-0.00051
C	3.82360	-1.61714	0.00049
C	3.81949	1.58776	-0.00030
C	-2.63021	0.73285	-0.00011
C	-2.62190	-0.70750	0.00049
C	-3.82354	1.61732	-0.00074
C	-3.81959	-1.58757	0.00032
H	4.75695	-1.05374	0.00901
H	3.80037	-2.28098	0.87257
H	4.74835	1.01841	-0.01121
H	3.80772	2.23690	0.88238
H	0.25328	2.70243	0.00030
H	-4.75691	1.05396	-0.00907
H	-3.81008	2.27066	0.87958
H	-3.80035	2.28099	-0.87296
H	3.81024	-2.27029	-0.87996
H	-4.74842	-1.01817	0.01062
H	-3.79656	-2.25189	0.87122
H	-3.80753	-2.23717	-0.88202
H	3.79612	2.25253	-0.87085
H	-0.25351	-2.70247	0.00034

a)



b)



$$g_x, g_y, g_z = 4.403, 1.960, 1.573 (S = 1/2)$$

Figure S13. a) The DFT optimized structure of square planar $\text{Co}(\text{Hdmg})_2$. b) Theoretical g factors and principal axes of $S = 1/2$ square planar $\text{Co}(\text{Hdmg})_2$ by NEVPT2.

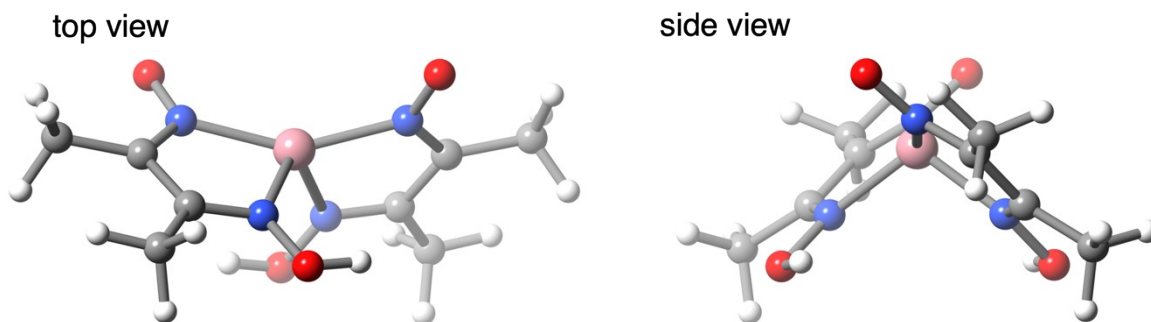
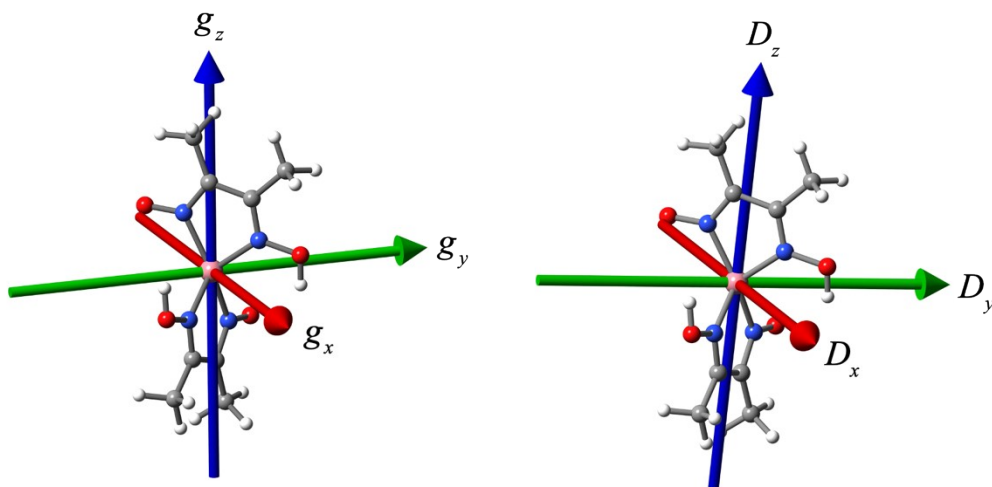


Figure S14. The optimized structure of $S = 3/2$ $\text{Co}(\text{Hdmg})_2$



$$g_x, g_y, g_z = 2.021, 2.025, 3.078 \quad (S = 3/2)$$

$$g_x, g_y, g_z = 0.085, 0.086, 9.046 \quad (\text{Kramer's doublet})$$

$$D = -91.969 \text{ cm}^{-1}$$

$$(E/D = 0.0119)$$

Figure S15. The theoretical g factors, zero-field splitting parameters, and principal axes of $S = 3/2$ distorted tetrahedral $\text{Co}(\text{Hdmg})_2$

DC magnetic experiments

Magnetization of 11% Co@Pd

The magnetization at 7T was found to be $\sim 0.7 \mu\text{B}$ per Co atom at 1.8 K, which is smaller than expected, similar to the case for 5% Co@Ni (Figure S16). The maximum around 4 K observed for the 11% Co@Pd is much more intense compared to 5% Co@Ni/Pd.

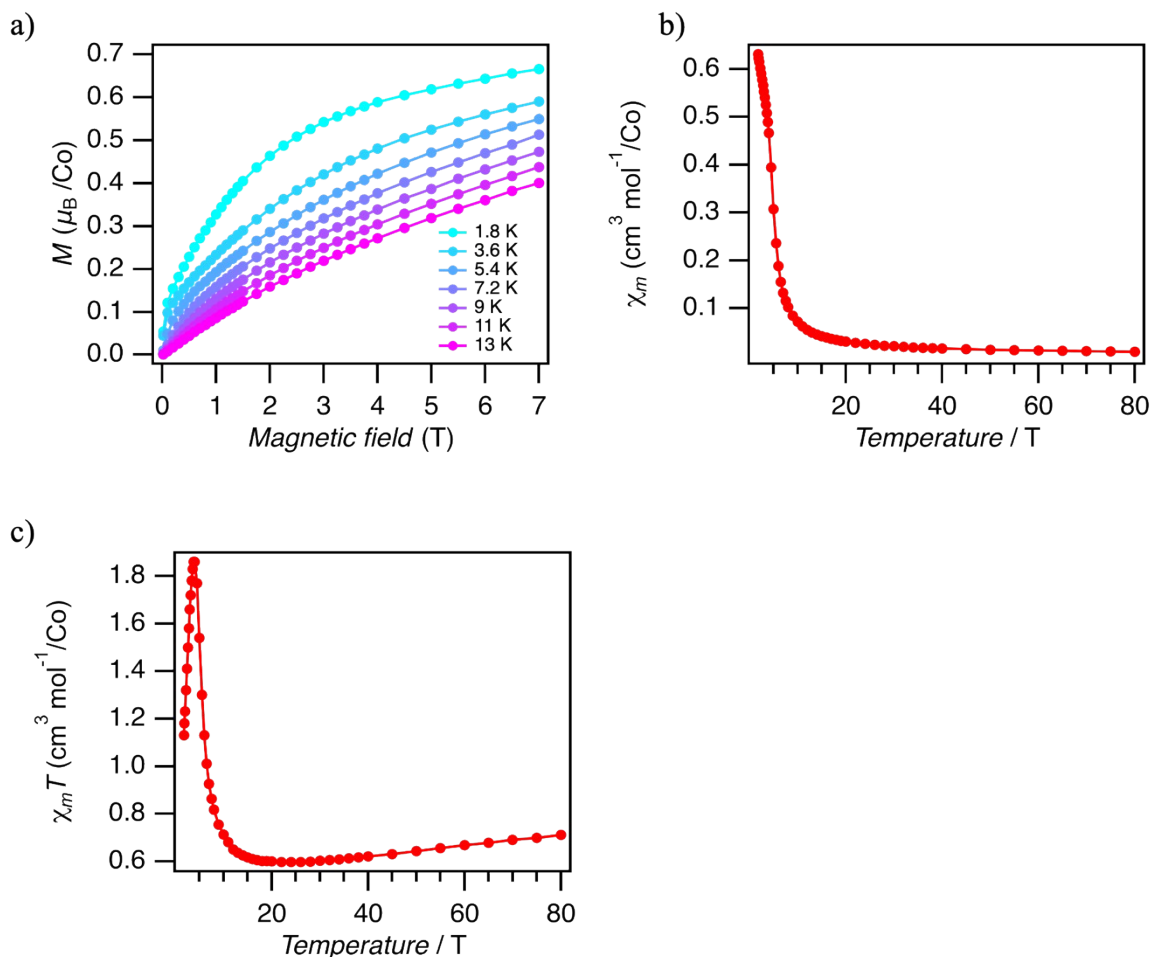


Figure S16. a) The Magnetization curves of 11% Co@Pd up to 7 T at 1.8 K to 13 K. b) The temperature dependence of susceptibility ($\chi_m T$) of 11% Co@Pd from 1.8 K to 80 K. c) The temperature dependence of susceptibility ($\chi_m T$) of 11% Co@Pd. The circles indicate the experimental data and the solid lines are visual guides.

Magnetization of 5% Co(II) in Pd(Hdmg)₂

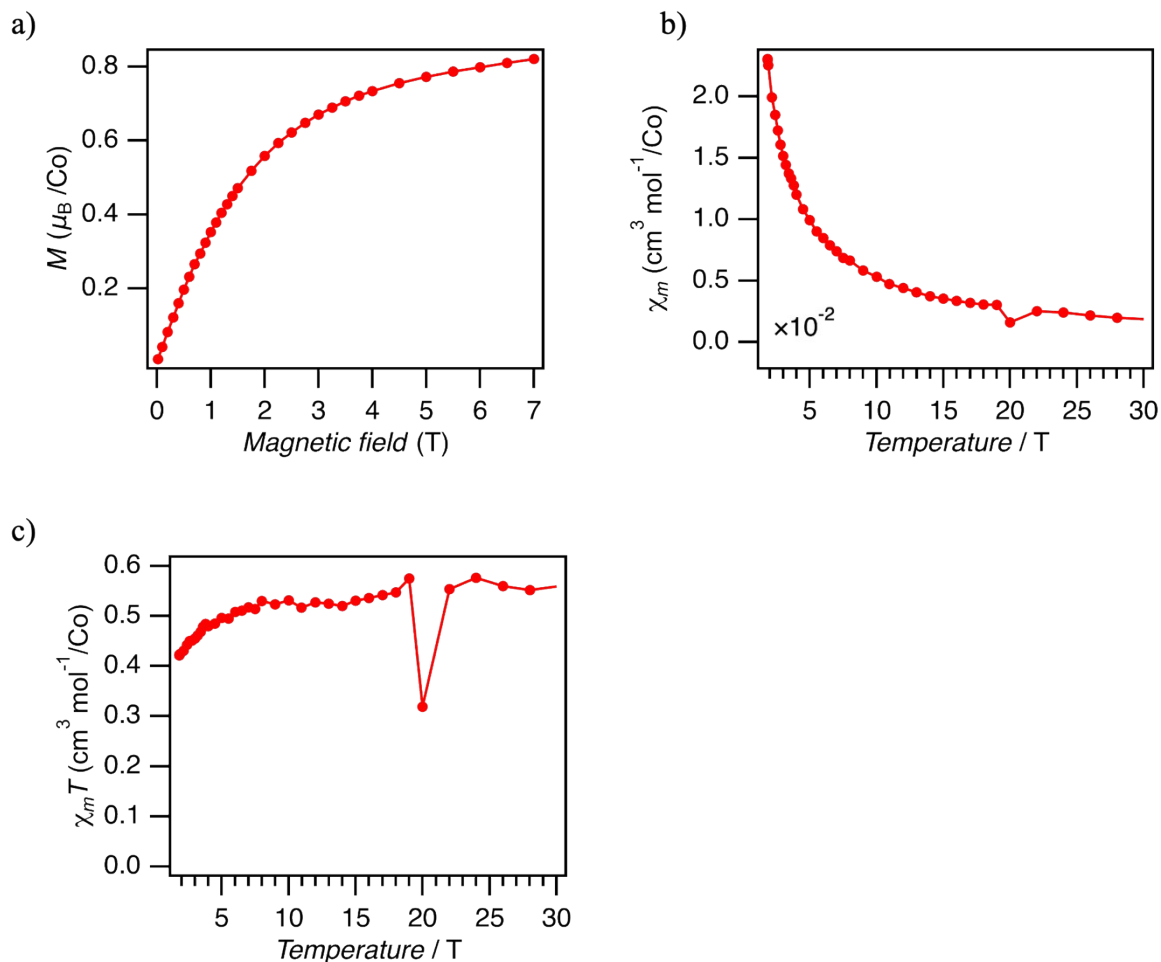


Figure S17. a) The magnetization curve of 5% Co@Pd up to 7T at 1.8 K. b) The temperature dependence of susceptibility (χ_m) of 5% Co@Pd. c) The temperature dependence of susceptibility ($\chi_m T$) of 5% Co@Pd. Red circles indicate the experimental data and the solid line is a visual guide.

The pure Co(Hdmg)₂ experiment

As described in the experimental section, Co(Hdmg)₂ synthesized in an Ar glove box was first dried under the Ar atmosphere, and the PXRD was measured. The elemental analysis () shows the compound synthesized is Co(Hdmg)₂ with two solvent molecules (EtOH(1-1) or MeOH(2-1)). Then to remove the solvent, the sample was dried under a vacuum at 80 °C following Schrauwzer's method¹. The elemental analysis of the evacuated samples(1-2, 2-2) shows agreement with the calculated CHN ratio of Co(Hdmg)₂ without any coordinating solvent. The PXRD measurement indicates the removal of solvents reduces the crystallinity of the compound significantly ().

Table S5. Elemental analysis results of pure Co(Hdmg)₂

	Found (Calc.) (%)			Formula
	C	H	N	
1-1	37.26 (37.8)	6.74 (6.88)	13.92 (14.69)	C ₁₂ H ₂₆ N ₄ CoO ₆ Co(Hdmg) ₂ •2EtOH
1-2	32.58 (33.23)	4.85 (4.88)	18.67 (19.28)	C ₈ H ₁₄ N ₄ CoO ₄ Co(Hdmg) ₂
2-1	34.07 (34.00)	6.33 (6.28)	15.85 (15.86)	C ₁₀ H ₂₂ N ₄ CoO ₆ Co(Hdmg) ₂ •2MeOH
2-2	33.12 (33.23)	5.00 (4.88)	19.11 (19.28)	C ₈ H ₁₄ N ₄ CoO ₄ Co(Hdmg) ₂

PXRD

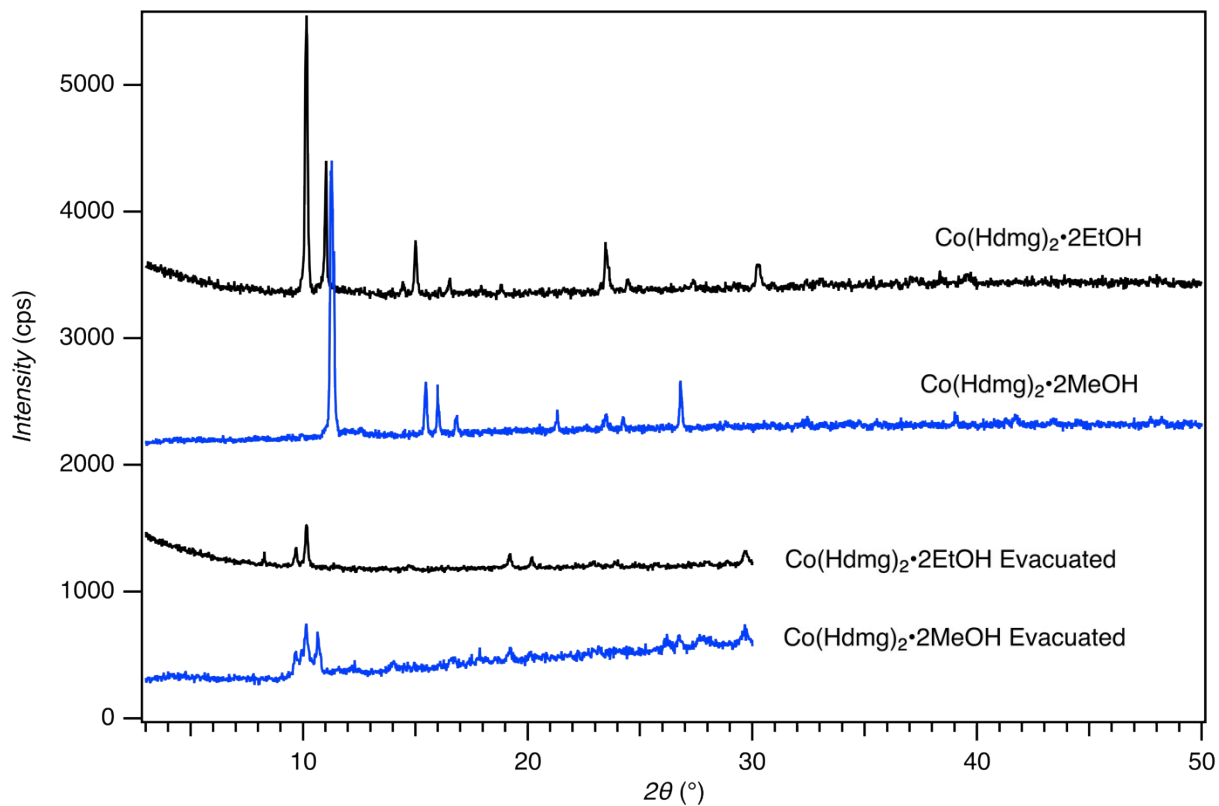


Figure S18. The PXRD pattern of pure Co(Hdmg)₂ before and after removing the EtOH (black) and MeOH (blue) solvent, respectively.

EPR spectroscopy

For the samples before vacuum drying, the CW-EPR spectra were obtained at RT as displayed in . Both the samples synthesized in MeOH and EtOH showed very similar spectra. The simulation of the $\text{Co}(\text{Hdmg})_2 \cdot 2\text{MeOH}$ is shown in (red) with the parameters in . The g factors obtained here () are quite close to the g factors of $\text{Co}(\text{Hdmg})_2$ in the MeOH solution ($g_1 = 2.02$, $g_2 = 2.207$, $g_3 = 2.317$)⁸. After evacuating the samples, the EPR signal disappears at RT. Therefore, the EPR spectra after evacuation were recorded at 10 K, shown in . Both the samples prepared in MeOH and EtOH gave essentially the same spectra. As discussed in the next section, from the SQUID measurements, the samples after vacuum drying consist of exchange coupled dimers and a small amount of monomeric impurities. From the magnitude of exchange coupling estimated from the magnetic data, at 10 K, a small amount of dimers exist as $S = 1$. In the case of both dimers, the hyperfine coupling should split into 15 lines due to two Co ($I = 7/2$) interactions. However, peaks do not seem to have split into 15 lines. This may be because the relaxation of this species is significantly fast and the spectrum becomes too broad to conceive any hyperfine splittings. The small splittings present in the spectra, which are quite similar to those of Co(II) in Ni/Pd(Hdmg)₂, especially around 350-400 mT, are probably from the monomeric impurities.

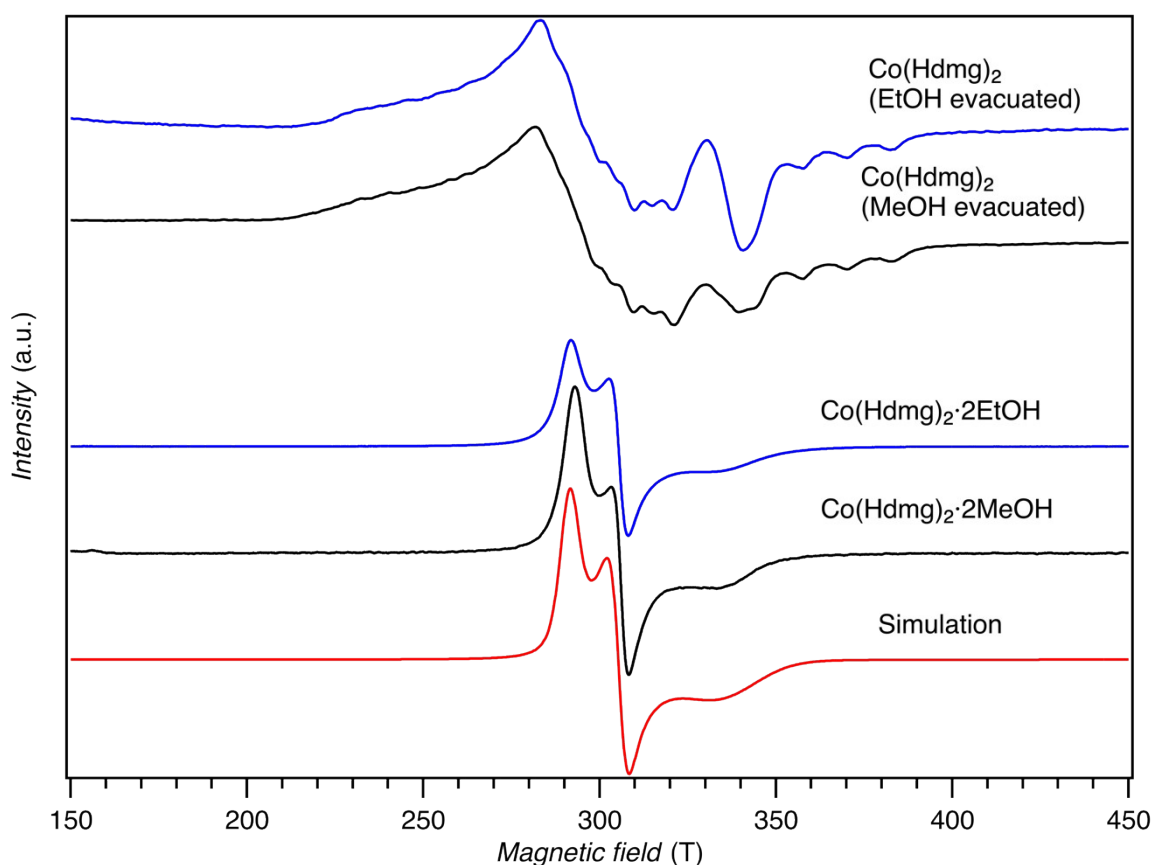


Figure S19. The X-band CW-EPR spectra of $\text{Co}(\text{Hdmg})_2$ before and after removing the solvent. The spectra of $\text{Co}(\text{Hdmg})_2 \cdot \text{MeOH}/\text{EtOH}$ were measured at RT. The spectra of the evacuated samples were taken at 10 K.

Table S6. Fitting parameters used in Easyspin

g	Line width (Gaussian)	Line width (Lorentzian)	g strain
(2.007, 2.206, 2.313)	2.8	2	(0.133, 0, 0.02)

Magnetic measurements

a) shows the magnetization curve obtained for $\text{Co}(\text{Hdmg})_2 \cdot 2\text{MeOH}$. For $\text{Co}(\text{Hdmg})_2 \cdot 2\text{MeOH}$, the magnetization at 7 T is smaller than expected for $S = 1/2$ with g factors obtained for this compound. The magnetization curve has a distinctive shape that cannot be fit by a simple Brillouin function. To account for the smaller magnetization than expected, dimeric species with $J = -21 \text{ cm}^{-1}$ that will be discussed below for the $\text{Co}(\text{Hdmg})_2$ after the solvent removal was taken into consideration for the fitting. This species has essentially no significant contribution to the magnetization as shown in b). Therefore, the shape of the curve cannot be reproduced well with only the addition of the dimeric species to the isolated $S = 1/2$ $\text{Co}(\text{Hdmg})_2 \cdot 2\text{MeOH}$. In order to have a better agreement with the experiment, another exchange-coupled species of $J = -6.5 \text{ cm}^{-1}$ was introduced. The best fit was obtained with 49% of the monomer, 31% of the $J = -21 \text{ cm}^{-1}$ dimer, and 20% of another exchange coupled species as shown in the solid line in a).

The sealing of the sample was carried out under vacuum, which might cause some of the solvent molecules to be pulled off, causing dimeric species of $J = -21 \text{ cm}^{-1}$ as in the fully dried samples. It is not clear why the partial inclusion of $J = -6.5 \text{ cm}^{-1}$ was necessary. However, multiple interactions were required to fit the magnetic data, similarly for $\text{Co}(\text{salen})$ systems which is analogous to $\text{Co}(\text{Hdmg})_2$, and this was ascribed to interdimer and intradimer interactions and also to a mixture of species in different structures¹⁴.

The susceptibility data is shown in b) and c). However, it was difficult to get reliable data by accurate diamagnetic correction due to large diamagnetic contributions from an NMR tube and eicosane to protect the sample from the oxygen and fix the solid inside the tube. We subtracted the experimentally obtained diamagnetic data of the NMR tube, eicosane, and Pascal's diamagnetic correction of the measured complex but we cannot be confident about the accuracy of the data. Therefore further analysis will not be discussed. Even though we included the antiferromagnetic dimers in our fitting, both the experimental data and the χ_m vs T curve do not show any maximum probably hidden by other paramagnetic signals.

For $\text{Co}(\text{Hdmg})_2$, after solvent removal, a significant reduction of magnetization was observed as shown in a). This suggests the removal of the solvents generated antiferromagnetically coupled species, probably dimers similar to $[\text{Co}(\text{salen})]_2$.

The χ_m vs T curve is shown in d). Again, due to a large diamagnetic contribution, the absolute values are not reliable. However, in line with the reduced magnetization, it shows a maximum, which is characteristic of antiferromagnetically coupled materials. This maximum in the χ_m curve was always present even before the diamagnetic correction, suggesting that it is not an artifact due to the diamagnetic correction. The rise of the χ_m value below 10K is likely to arise from monomeric impurities as seen in the $[\text{Co}(\text{salen})]_2$ case¹⁴.

The χ_m vs T data in d) was fitted well with $J = -21.8 \text{ cm}^{-1}$, a similar value obtained for dimeric $[\text{Co}(\text{salen})]_2$. This suggests that the antiferromagnetically exchanged coupled species in $\text{Co}(\text{Hdmg})_2$ is probably in a similar dimeric form to $[\text{Co}(\text{salen})]_2$. As stated, the absolute values of experimental χ_m are not reliable due to uncertainties in diamagnetic correction. It is also not clear if the dimeric $\text{Co}(\text{Hdmg})_2$ is the only species present in the sample aside from a small amount of monomeric impurity. Therefore, only the curve shape was fit with some multiplication factors applied to the simulated curve. In d), the simulated χ_m value in a solid blue line was multiplied by

0.38. Based on the magnitude of exchange coupling in the dried sample, we attempted the fitting of the magnetization curve too. The antiferromagnetically coupled species has significantly small magnetization and has almost no contribution to the magnetization with magnetization on the order of 10^{-6} at 7 T as shown in b). The observed small magnetization of ~ 0.02 in a) probably comes from monomeric impurities. The magnetization curve in a) can be fitted with somewhat good agreement by considering 2% of monomeric impurities in addition to the dimers. It is not clear whether the difference between the fit and experiment is due to errors in diamagnetic correction or other magnetic impurities that are not taken into consideration.

To sum up, aside from slight impurities, the solvent removal causes a significant reduction of magnetization and the appearance of a maximum in the χ_m vs T curve. This clearly indicates that $\text{Co}(\text{Hdmg})_2 \cdot 2\text{MeOH}$ forms antiferromagnetically coupled dimers similar to $[\text{Co}(\text{salen})]_2$ when the axially coordinated solvents are removed.

$\text{Co}(\text{Hdmg})_2 \cdot 2\text{MeOH}$

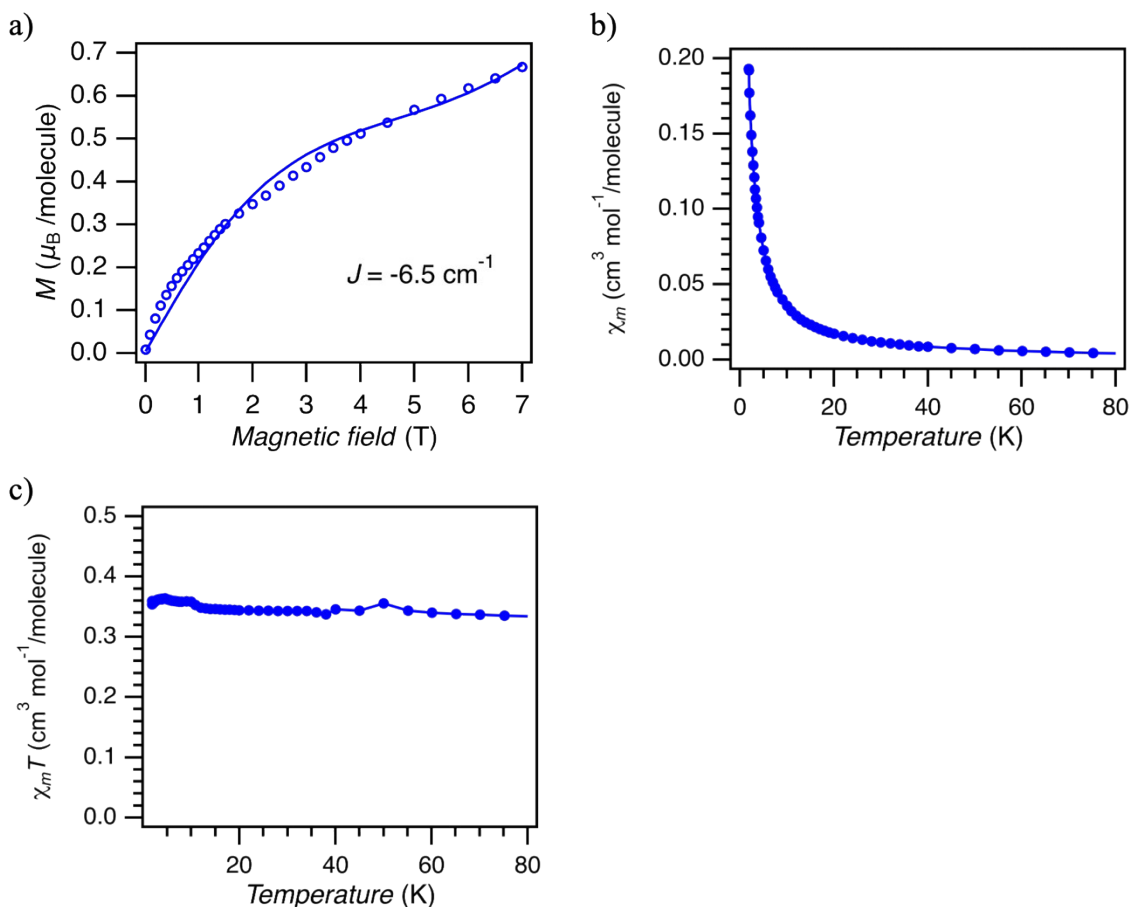


Figure S20. a) The magnetization curve of the $\text{Co}(\text{Hdmg})_2 \cdot 2\text{MeOH}$ at 1.8 K. The open circle shows the experimentally obtained data, and the solid line indicates the fitting result. b), c) DC susceptibility ($\chi_m, \chi_m T$) of the $\text{Co}(\text{Hdmg})_2 \cdot 2\text{MeOH}$ measured under a magnetic field of 1000 Oe.

Co(Hdmg)₂•2MeOH after solvent removal

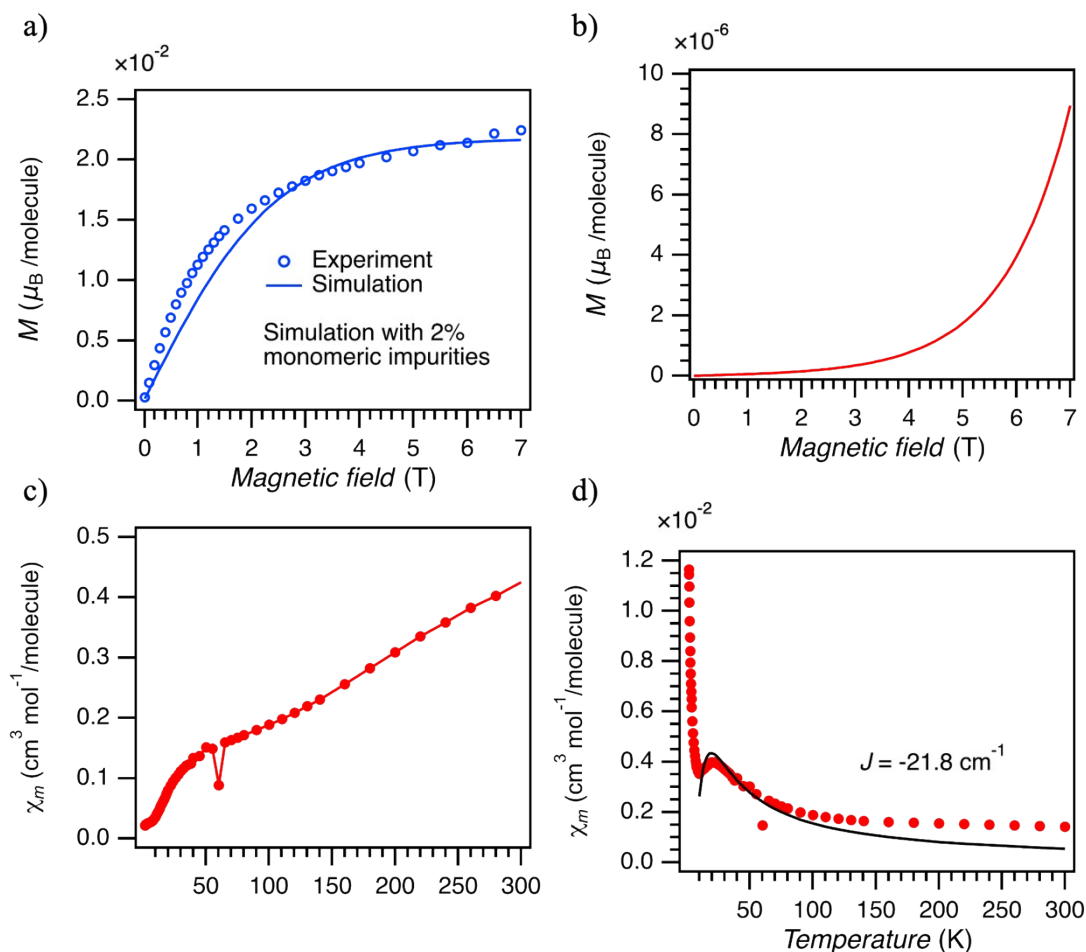


Figure S21. a) Magnetization curve Co(Hdmg)₂•2MeOH after solvent removal. 2% of monomeric impurities gave the best fit for the experimental curve. The g factors are taken from the EPR spectra, assuming that the g factors of the dimer and monomer are similar. b) The simulated magnetization curve of antiferromagnetically coupled dimers with $J = -21.8 \text{ cm}^{-1}$. c) Temperature dependence of $\chi_m T$ d) Temperature dependence of χ_m of Co(Hdmg)₂•2MeOH after solvent removal. The best fit for the maximum was obtained with $J = -21.8 \text{ cm}^{-1}$.

AC susceptibility

Before the solvent removal, in the AC susceptibility, field-induced magnetic relaxation was observed as in . This is consistent with the EPR spectrum in , which indicates Co(Hdmg)₂ with solvents is $S = 1/2$. After the solvent removal, the AC signal was not observed even with an applied magnetic field. This is consistent with the other experimental data that shows the removal of solvents induces antiferromagnetically exchange-coupled dimeric Co(Hdmg)₂ with the ground state $S = 0$. The amount of the monomeric impurities or excited state $S = 1$ may be too small to be observed by our SQUID machine.

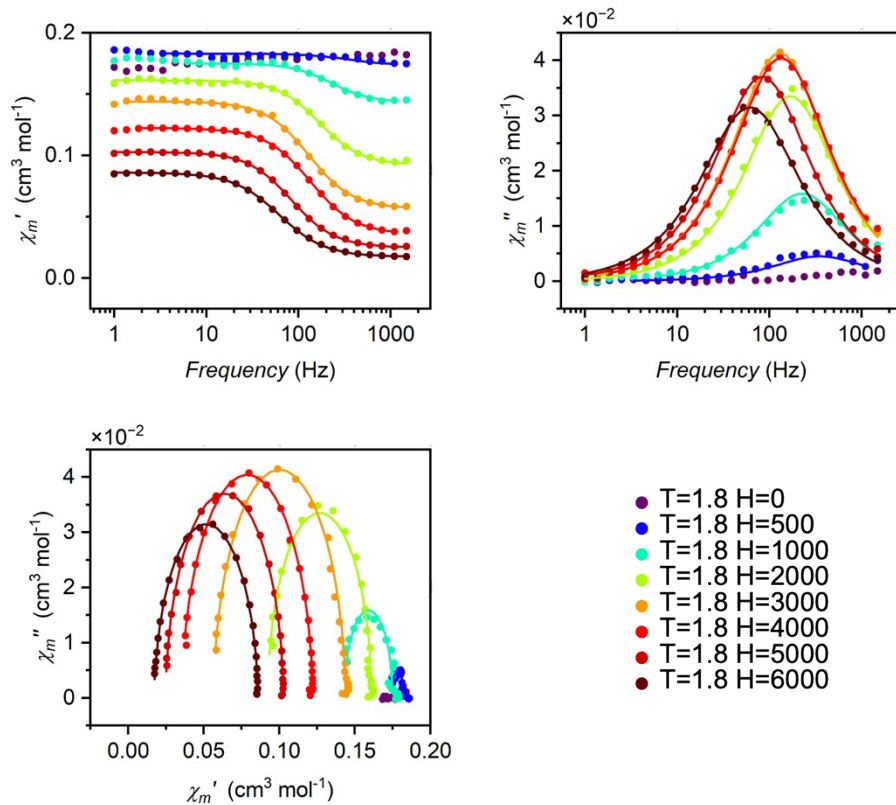


Figure S22. Field-dependence AC susceptibility of $\text{Co}(\text{Hdmg})_2 \cdot 2\text{MeOH}$ from 0-6000 Oe. χ_m'' peak was not observed at zero field.

Oxygen exclusion and magnetic measurements

The reduced magnetization might be due to a partial oxidation of the sample, turning Co(II) into diamagnetic Co(III). To test the hypothesis, Co@Ni was synthesized in an Ar glove box and sealed in an NMR tube for magnetic measurements without exposing the sample to air. The magnetization in Figure S23 showed a similar value to the experiments under air both for Co@Ni and Co@Pd. The slightly larger magnetization compared to those measured under air in a gelatine capsule can be attributed to the errors in the diamagnetic correction. The NMR tubes used for the air-free measurement have a much larger diamagnetic contribution to the capsules compared to the small signal coming from the tiny amount of dopant Co(II). This made the paramagnetic signal and the diamagnetic signal the same order of magnitude. For the same reason, it was not possible to obtain reliable temperature dependence susceptibility, with diamagnetic contribution quickly surpassing the paramagnetic signal. For the AC susceptibility, the zero field relaxation was also observed as shown in Figure S24, excluding the possibility that the origin of this relaxation is relevant to oxidation.

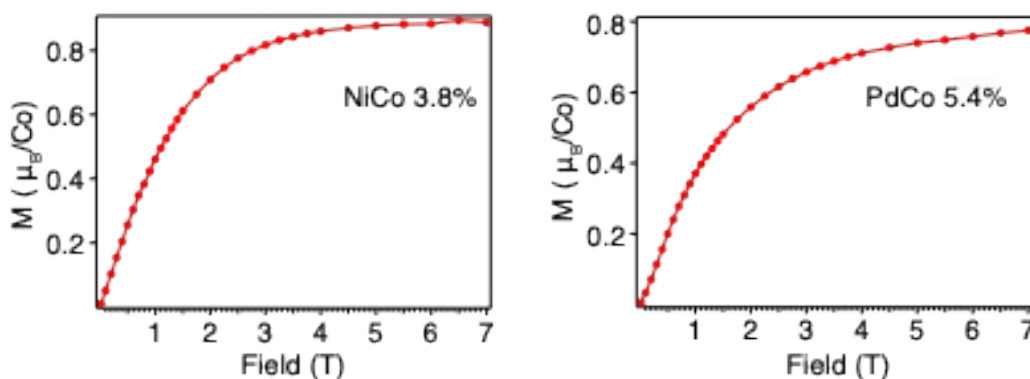


Figure S23. The magnetization of CoNi and Co@Pd matrix. The concentration of Co was found to be 3.8% and 5.4% for Ni and Pd respectively.

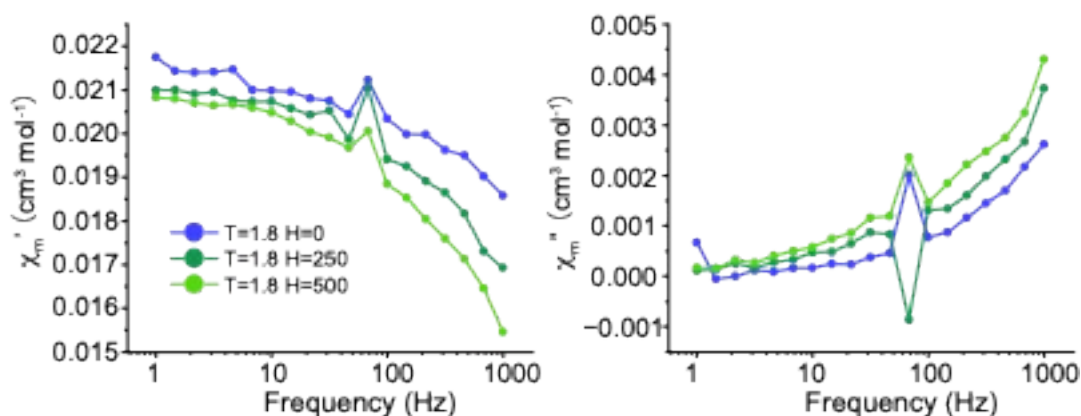


Figure S24. Field dependence AC susceptibility of 3.8% Co@Ni from 0 Oe to 500 Oe without air contact. Zero field relaxation was observed.

Simulation of magnetic data

Simulation of susceptibility with different ratios of exchange coupled dimers and $S = 1/2$

The below shows the simulated χ_m values by the Easyspin program with different ratios of dimers and monomers. The g factors for the monomer are taken from the simulation of the 5% Co(II) in Ni(Hdmg)₂ EPR spectrum. The same g factors are used for the dimers and exchange coupling of $J = -21 \text{ cm}^{-1}$, which was found in the pure Co(Hdmg)₂ was introduced in . The maximum from the dimers becomes invisible when the ratio of dimers is less than 60%.

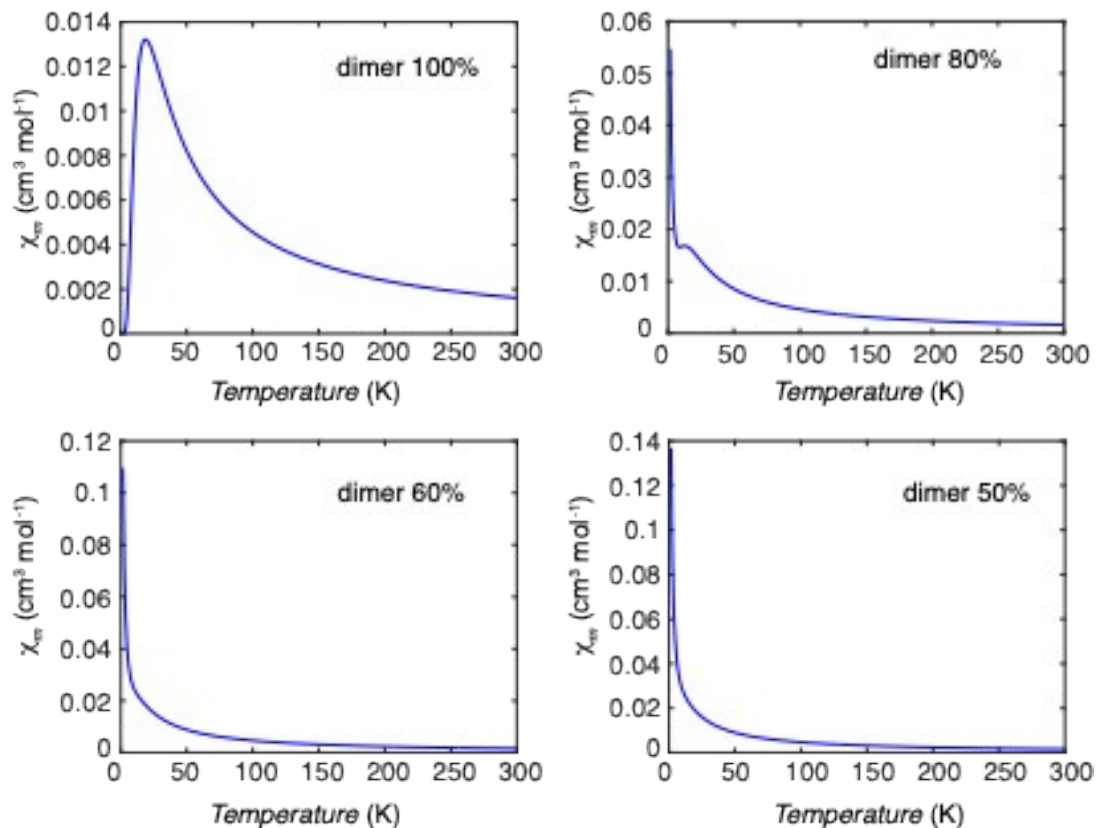


Figure S25. The simulations of χ_m with different ratios of dimers and monomers.

AC susceptibility

5% Co@Ni

The AC susceptibility was re-measured up to 1.5 T in addition to the susceptibility data in the main manuscript.

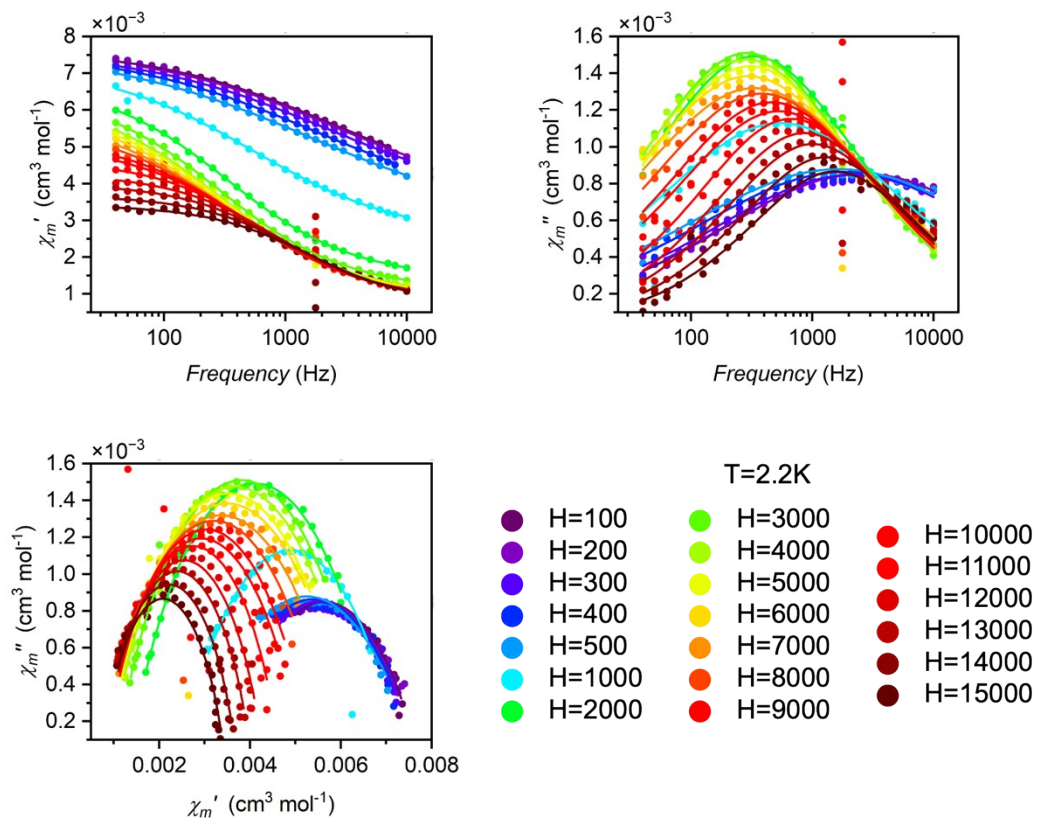


Figure S26. Field dependence AC susceptibility of 5% Co@Ni.

For 5%CoNi, we measured AC susceptibility at 3000 Oe as a function of temperature. We did not see any additional contribution from what we observed at 1.8 K, which is already shown in the manuscript.

The lack of contributions from other magnetic centers can be explained by the shorter spin-lattice relaxation and the detection limit of the measurement. Though we do have several magnetic centers, they do not necessarily appear in the AC susceptibility. For example, for the planar motif (1), the spin-relaxation is expected to be much faster than the heterometallic dimer due to larger spin-orbit coupling, as can be seen from the larger deviations of g factors from the free electron value. Therefore, the AC susceptibility of this species probably falls out of the range of measurements (up to 10000 Hz). We also note that the number of spins in our samples is already quite low due to the dilution in the diamagnetic matrices. Therefore, we can only see the major magnetic species in our sample due to the detection limit of MPMS and PPMS.

The absence of contribution from the homometallic dimer in the triplet state can also be explained by the low number of spins, as they are mostly in the singlet state at low temperatures. Though with higher temperatures, the amount of the triplet state increases, the spin-lattice relaxation can fall out of the measurable range at the higher temperature.

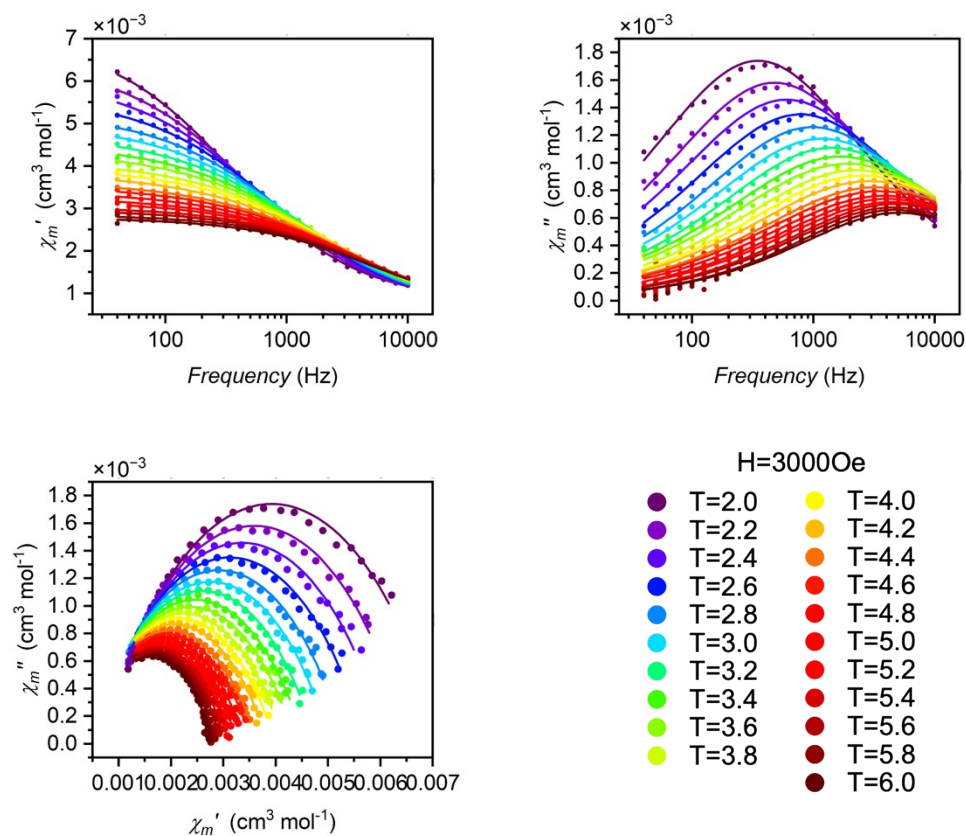


Figure S27. Temperature dependence AC susceptibility of 5% Co@Ni under 3000 Oe.

5% Co@Pd

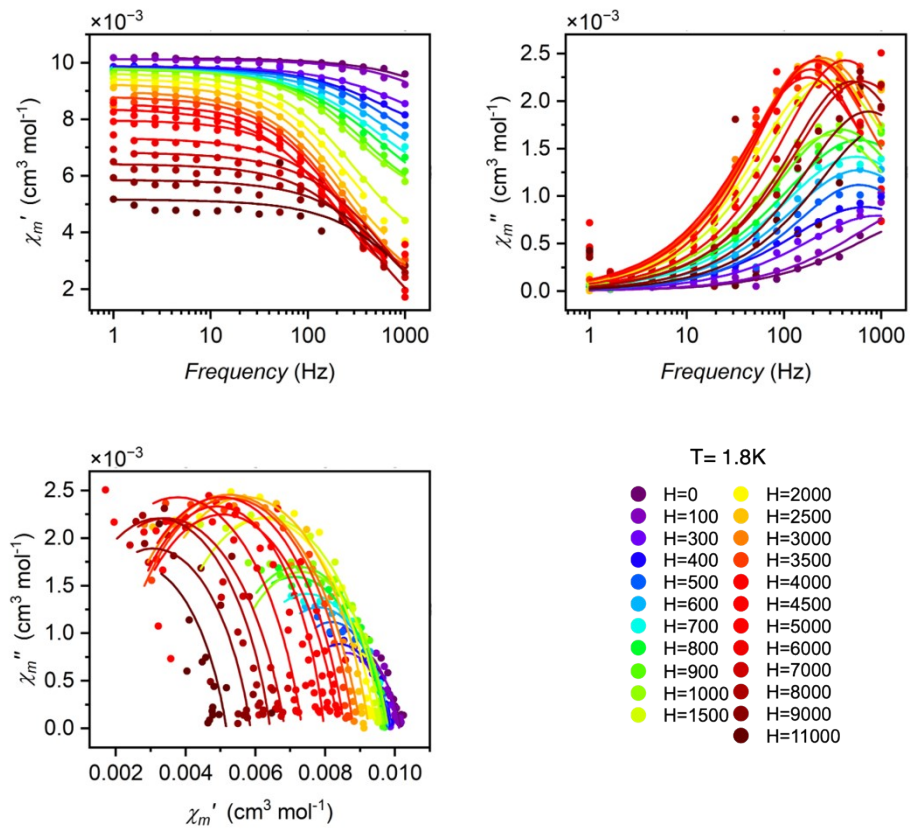


Figure S28. Field dependence AC susceptibility of 5% Co@Pd

11%Co in Pd(Hdmg)₂

Consideration of two relaxation processes was required to fit the data for the 11% Co@Pd from 700 Oe to 1000 Oe as in Figure S30.

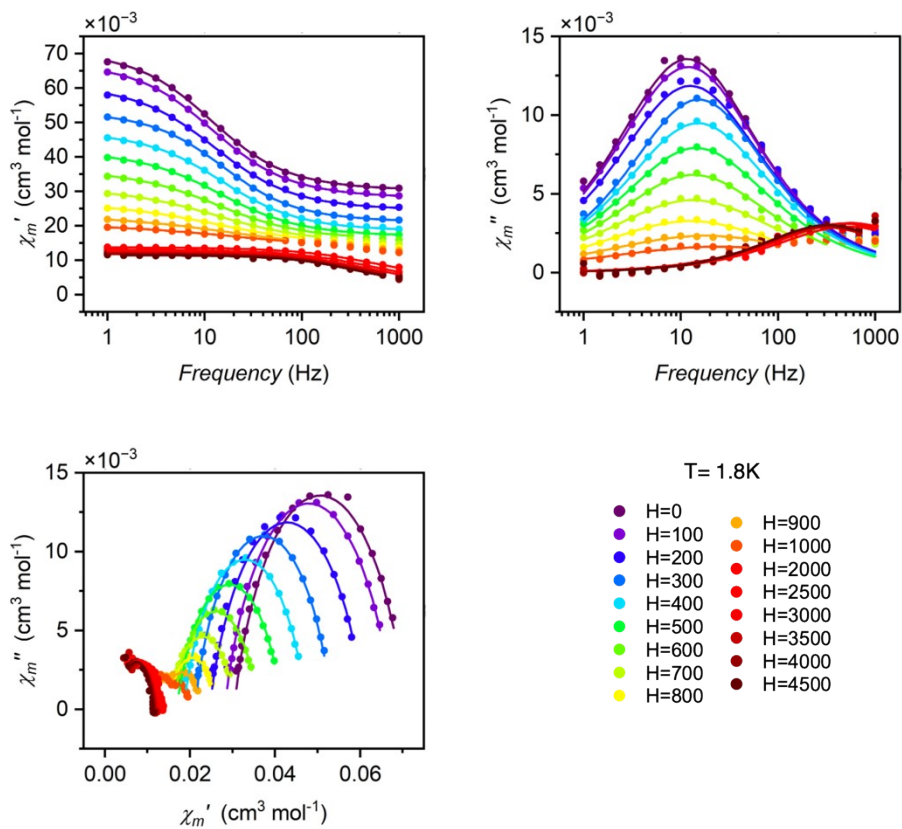


Figure S29. Field dependence AC susceptibility of 11% Co@Pd

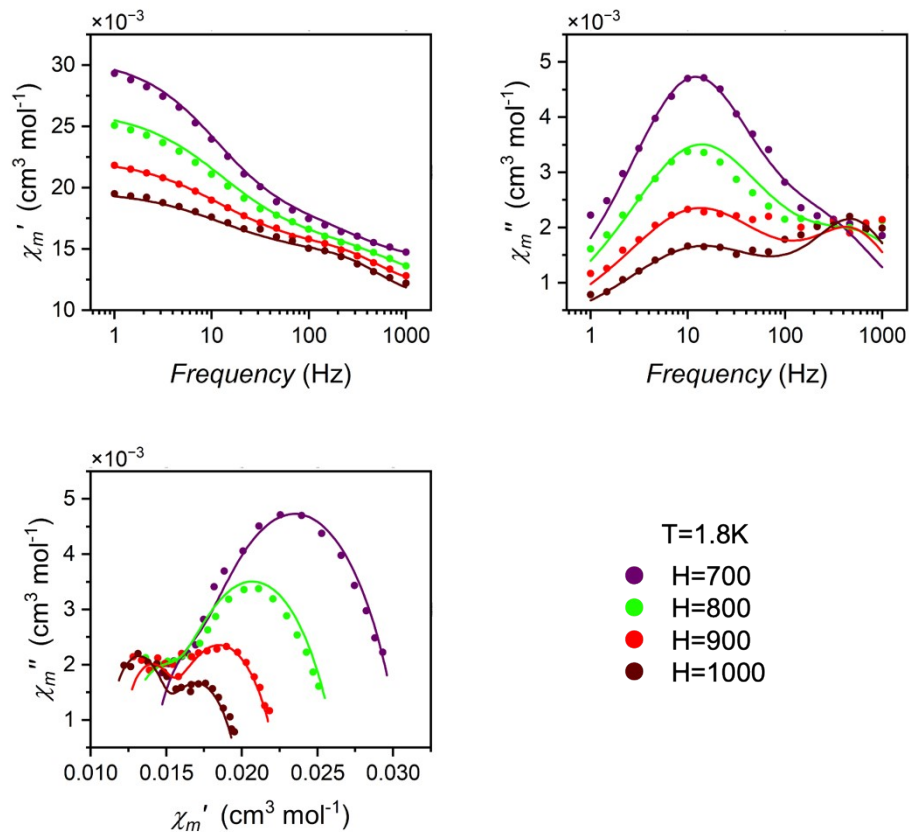


Figure S30. Fitting by two relaxation processes of 11% Co@Pd

Field dependence of relaxation times of 5% CoNi and 5% CoPd

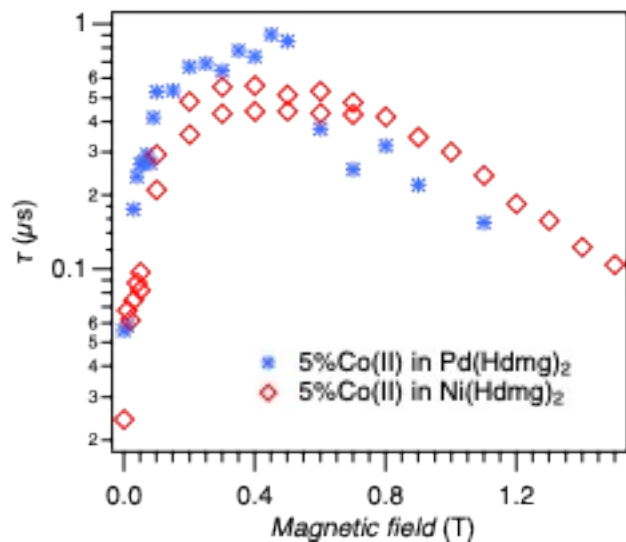


Figure S31. The field-dependent relaxation time obtained by fitting the AC susceptibility for 5% Co@Ni and Co@Pd. The relaxation times for 5% Co@Ni were taken from two different measurements shown in the manuscript and Figure S26.

Spin-glass experiment

To investigate the possibility of spin glass behavior, as suggested by the zero-field relaxation and the magnetic interactions inferred from DC magnetic measurements, the temperature dependence of AC susceptibility was measured for the 11% Co@Pd, as shown in Figure S32. The temperature dependence shows a cusp around 4 K in the in-phase component (χ'). This peak shifted slightly to higher temperatures as the AC excitation frequency increased. For 5% Co@Ni and Co@Pd samples, the χ' peak was the accessible temperature range (below 1.8 K), preventing the study of frequency dependence for these samples (Figure S37). The frequency-dependent peak shift can be evaluated using the Mydosh parameter ϕ (eq. 1), where T_1 and T_2 are the temperatures of the maximum in the in-phase component at frequency ν_1 and ν_2 . This parameter is commonly employed to distinguish spin glass behavior from superparamagnetic systems, such as single-molecule magnets (SMMs).

$$\phi = \frac{T_1 - T_2}{T_1(\log \nu_1 - \log \nu_2)} \quad \#(1)$$

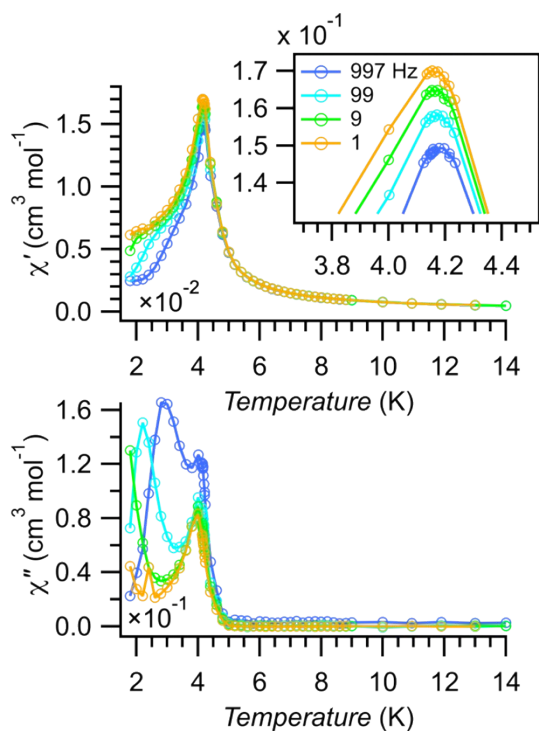


Figure S32. The temperature dependence of AC susceptibility of 11% Co@Pd. The top shows the in-phase component (χ') and the bottom shows the imaginary component (χ''). The inset on the top is a close-up of the in-phase component around the maxima.

The obtained Mydosh parameter (0.002) for 11% Co@Pd is significantly lower than the value typical for superparamagnets (~ 0.3)^{45,46}, further supporting that the zero-field relaxation is due to spin glass rather than a high spin Co(II) SMM.

Zero-field cooled and field-cooled DC magnetic susceptibility as a function of temperature was also measured at a small magnetic field (Figure S33 for 11% Co@Pd, Figure S38 for 5% Co@Ni/Pd). All of the samples show a bifurcation below around 4 K. The less concentrated 5% Co@Ni/Pd samples show a much less pronounced difference between ZFC and FC and the ZFC susceptibility continuously increases with lowering the temperature without a clear maximum. The absence of maximum in the DC magnetic susceptibility in a very diluted spin glass system was observed previously. In fact, a similar change in the AC susceptibility by concentration was also observed with those of our 5% and 11% samples⁴⁷. In the AC susceptibility, they observed double maxima in χ' , and the relative intensity of the maxima changes with the concentration; as the concentration decreases, the maximum at the lower temperature starts to dominate. They concluded that the two maxima have different origins; the higher temperature maximum is due to interactions of intermediate strength within a cluster and the lower temperature maximum comes from long-range dipole-dipole interactions between separated clusters. At a closer look at our data in Figure S32, there is a small maximum in χ' at lower temperatures (around 1.8-2 K) with maxima in χ'' as well. In the diluted 5% sample (Figure S37), the increase of χ' can be observed around this temperature and the trend is very similar to the previous concentration study. Therefore, the decrease of the maximum temperature in the 5% samples compared to the more concentrated 11% Co@Pd is probably due to the weaker interaction between clusters and the dominating interaction changes to weak long-range dipole-dipole interaction as the separation of each cluster becomes larger with decreasing the Co(II) concentration.

In addition to the conventional ZFC measurement, the aging effect under a magnetic field was studied by following the established procedure⁴⁸. In this procedure, the ZFC susceptibility is measured with intermediate stops on heating. Figure 8 shows the ZFC susceptibility measured based on the reported procedure with intermittent halts at various temperatures for 1 h while heating. During the waiting time, the gradual growth of susceptibility was observed, which indicates a relatively slow dynamic of spins. When the heating is re-initiated, the susceptibility increases less steeply, merging with the original curve that was measured without any stops. This behavior is known as a characteristic aging effect of spin glass⁴⁸⁻⁵¹.

Overall, the small Mydosh parameter, and the aging effect observed by ZFC DC susceptibility point toward spin glass rather than superparamagnets, therefore we concluded that the relaxation we observed at zero-field is from a spin-glass state. In addition to well-isolated species identified by EPR spectroscopy, both the DC and AC SQUID magnetic measurements indicate that Co(II) distribution in the Ni/Pd(Hdmg)₂ matrices are not homogeneous with highly Co(II) concentrated areas despite dilution. This is likely due to the properties to form dimers and other polymers of Co(Hdmg)₂, as discussed in the synthesis section.

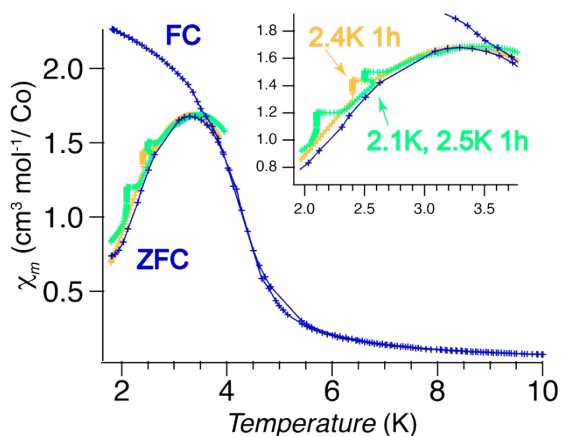


Figure S33. The blue line shows the ZFC and FC DC susceptibility (χ_m) under 100 Oe as a function of temperature for 11% Co@Pd without any intermittent stops. The cooling rate was 2 K/min and the heating rate was 0.5 K/min. The orange and green lines are the ZFC DC susceptibility with intermittent stops at 2.4 K, 2.1K, and 2.5 K for 1h at each temperature, respectively. The cooling rate was 2 K/min and the heating rate was 0.1 K/min.

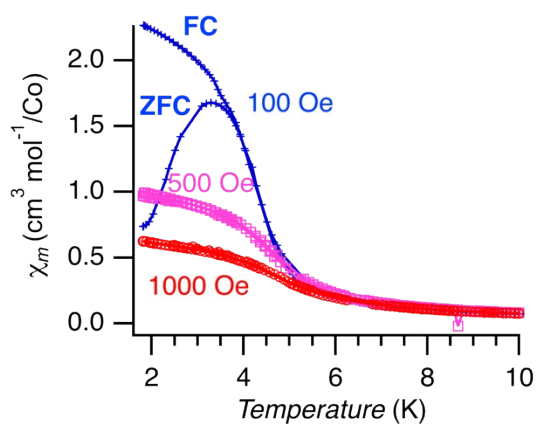


Figure S34. ZFC and FC DC susceptibility (χ_m) as a function of temperature for 11% Co@Pd under different magnetic fields up to 1000 Oe.

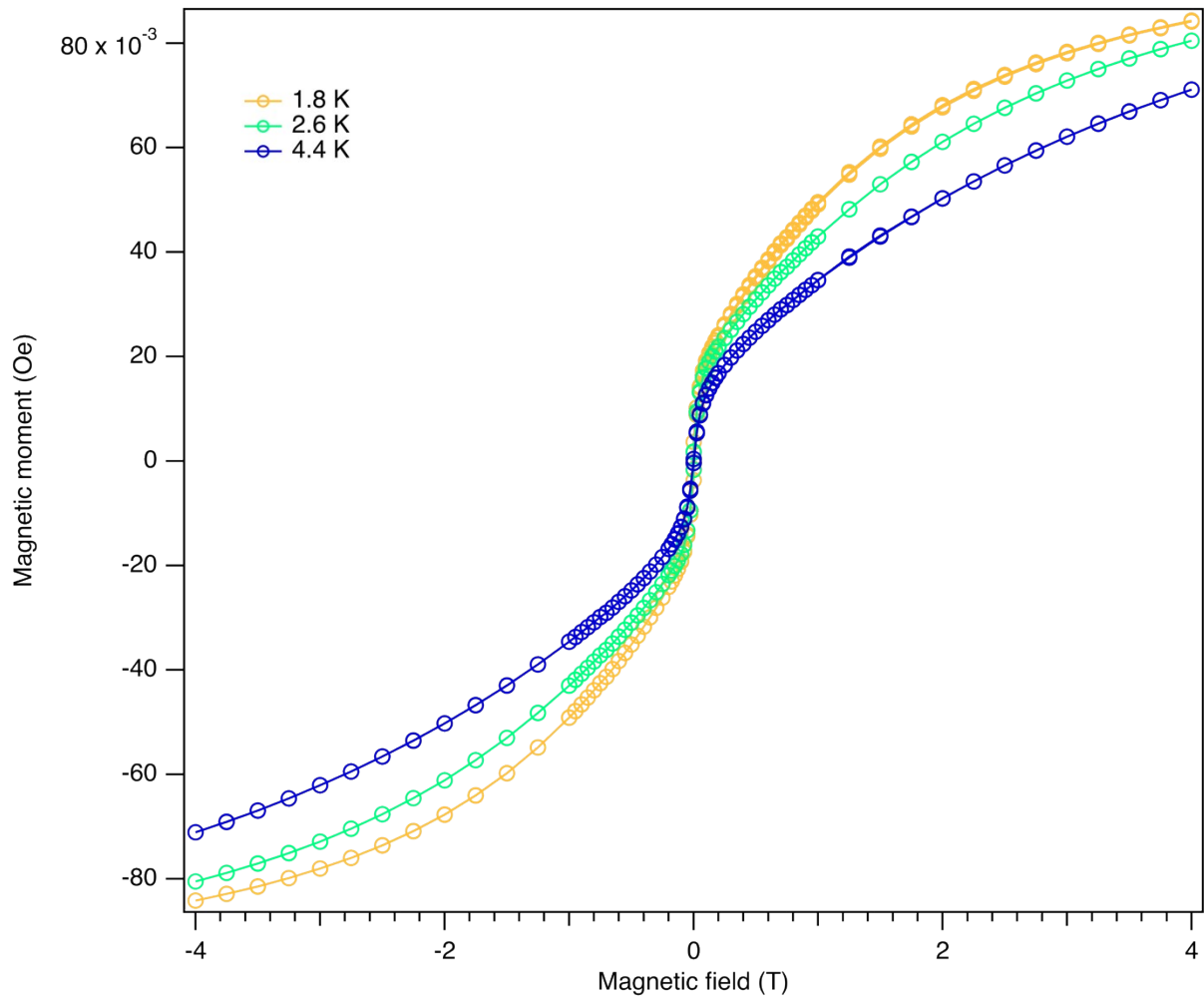


Figure S35. Hysteresis loop of 11% Co@Pd at 1.8 K, 2.6 K, and 4.4 K.

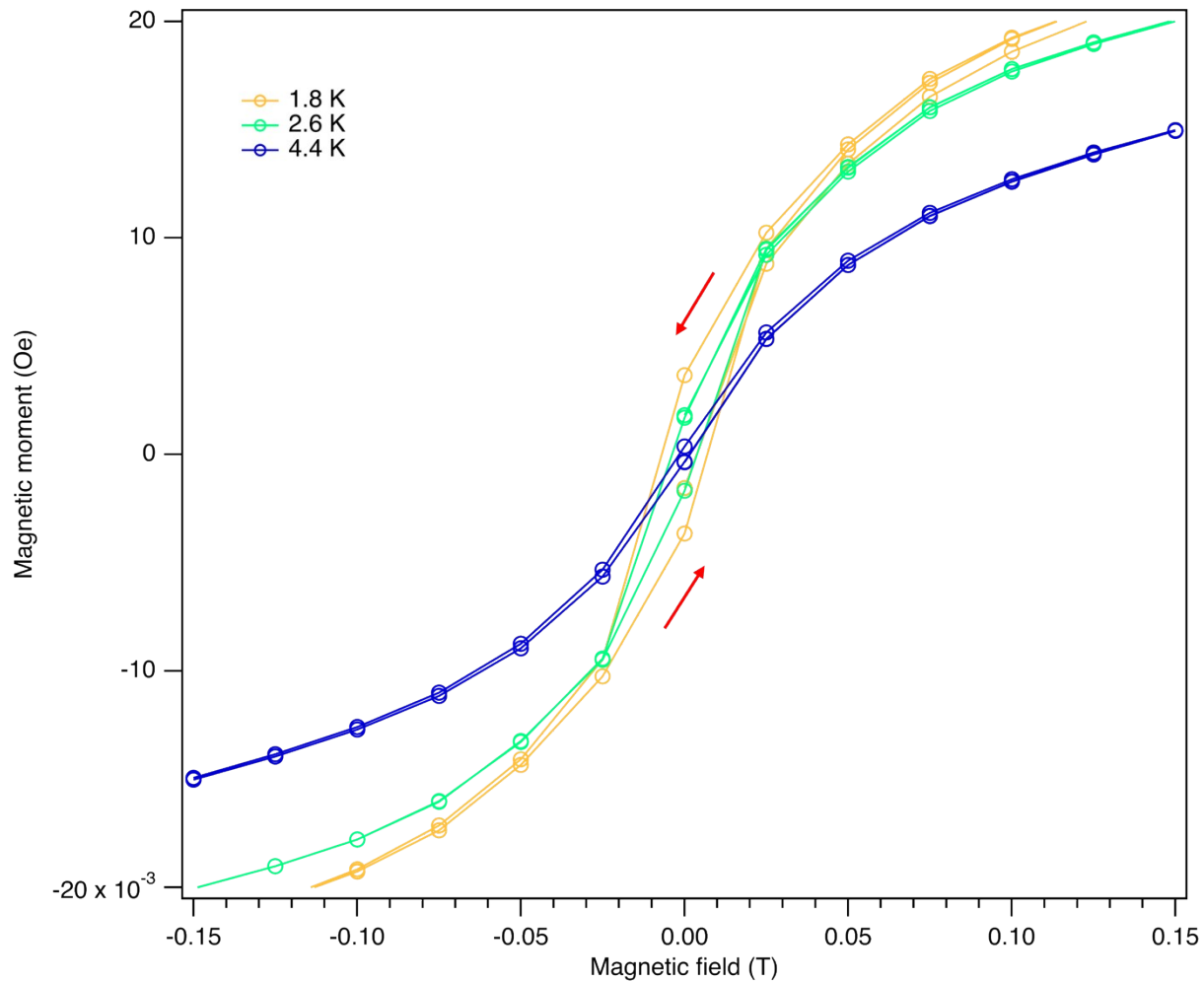


Figure S36. Hysteresis loop of 11% Co@Pd. The closer look at a lower magnetic field region.

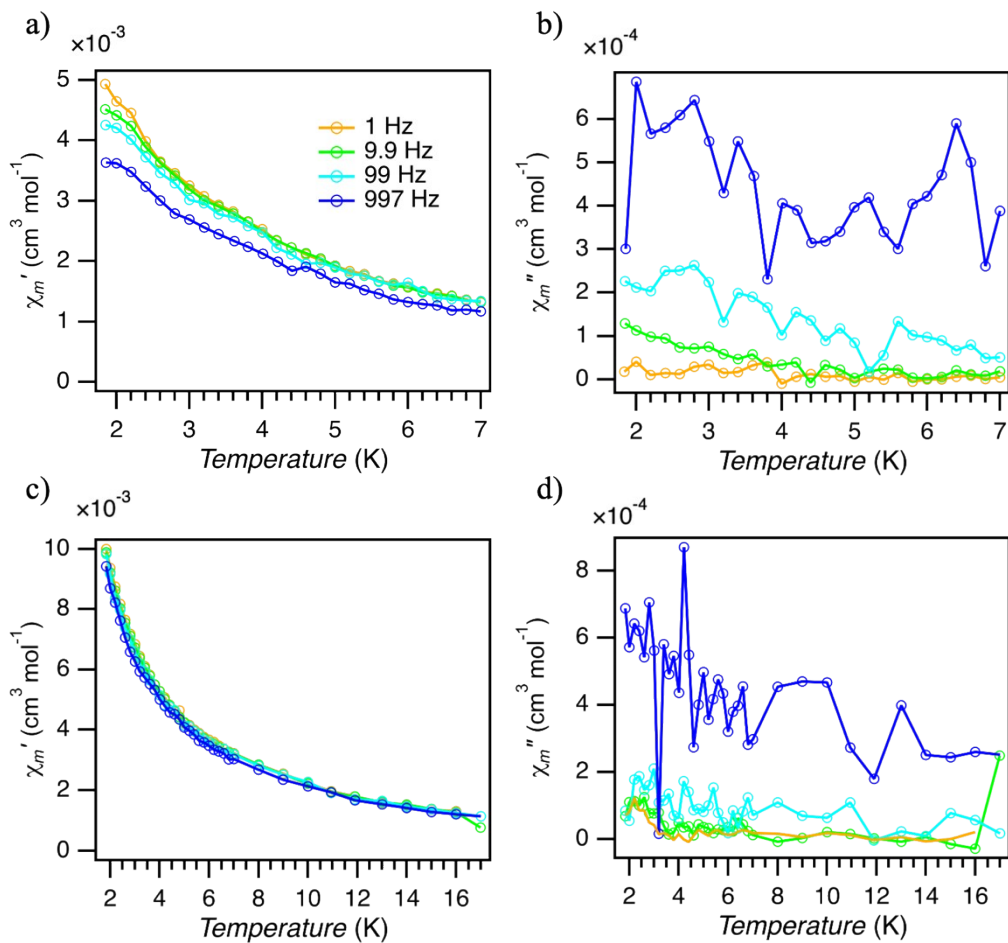


Figure S37. The temperature dependence of AC susceptibility with the excitation frequency of 1 Hz (orange), 9.9 Hz (green), 99 Hz (cyan), and 997 Hz (blue). The in-phase component of a) 5% Co@Ni and c) 5% Co@Pd. The imaginary component of b) 5% Co@Ni and d) 5% Co@Pd

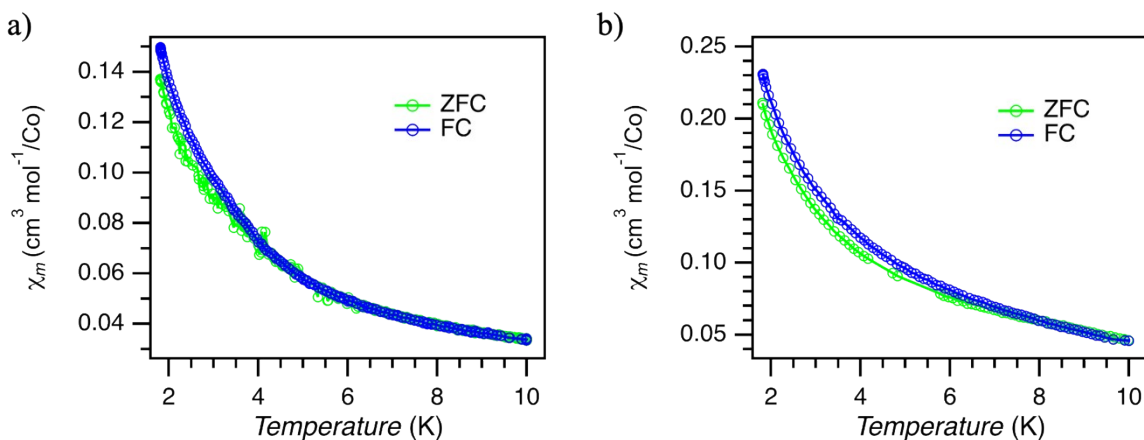


Figure S38. ZFC, FC dc susceptibility (χ_m) as a function of temperature for a) 5% Co@Ni, b) 5% Co@Pd under a magnetic field of 25 Oe.

XANES spectroscopy

The edge of the Co_3O_4 , typically observed at 7709 eV⁵²⁻⁵⁵, was taken as the zero reference point for the spectra (Figure S39 a)). The XANES spectra of 5% Co@Ni at 10 K and 300 K show almost identical spectra and no significant structural change was observed by the temperature change from 10 K to 300 K (Figure S39 b)). The first peak at about one eV higher in energy to the reference is assigned to the $1s \rightarrow 3d$ transition. Another pre-edge peak at ~ 5 eV is assigned to the $1s \rightarrow 4p$ transition^{56,57}. A significantly intense peak is often observed for Co(II) in a square planar geometry, as exemplified by cobalt(II) porphyrin⁵⁶. In our case, this peak is relatively weak and the intensity is closer to that of Co(salen) and pyridine-coordinated Co(II) porphyrin. Therefore, the major Co(II) species in $\text{Ni}(\text{Hdmg})_2$ is likely to be in a 5-coordinate geometry.

11% Co@Pd was also subjected to XANES spectroscopy (Figure S39 c)), but the noise was significantly larger, likely due to the shielding effect of the heavier Pd atom. The peak positions of Co(II) in the Ni and Pd matrices were found to be the same (Figure S39 d)), suggesting the Co(II) local environment for the Co(II) in both the Ni and Pd matrices are essentially identical.

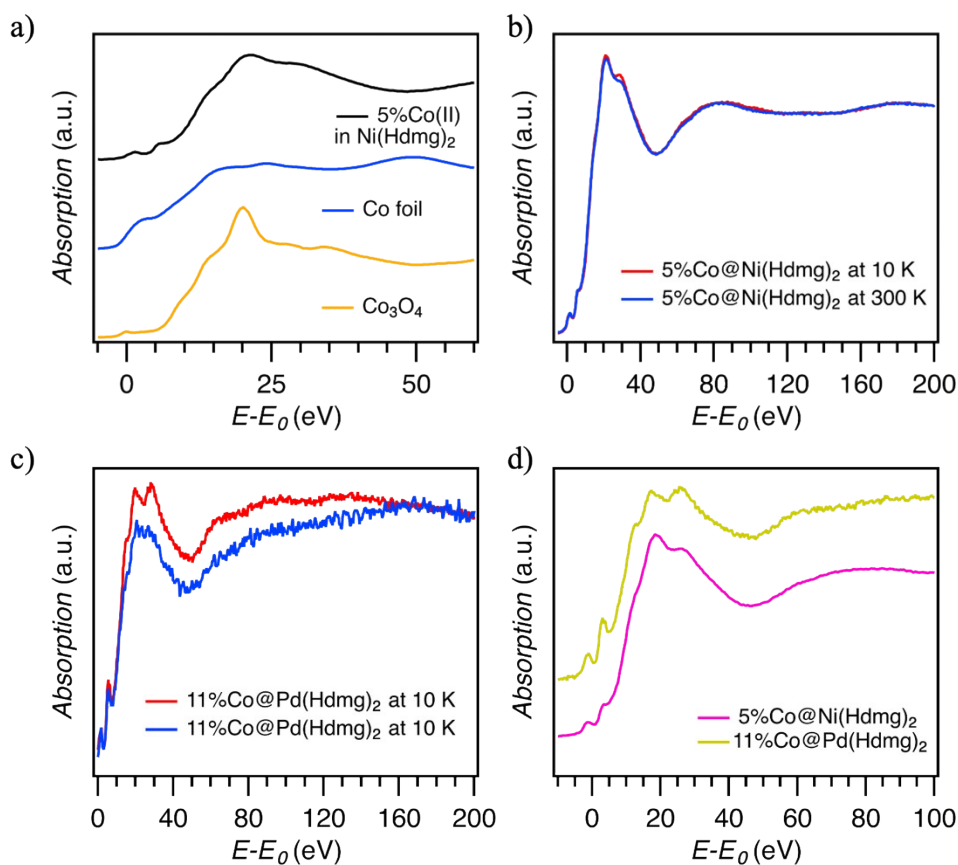


Figure S39. a) XANES spectrum of 5% Co@Ni at 300 K compared with the references of Co_3O_4 and Co foil. b) XANES spectra of 5% Co@Ni at 10 K (red) and 300 K (blue). c) XANES spectra of 11% Co@Pd at 10 K (red) and 300 K (blue). d) The comparison of XANES spectra of 5% Co@Ni and 11% Co@Pd.

Energy level diagram of clock transitions

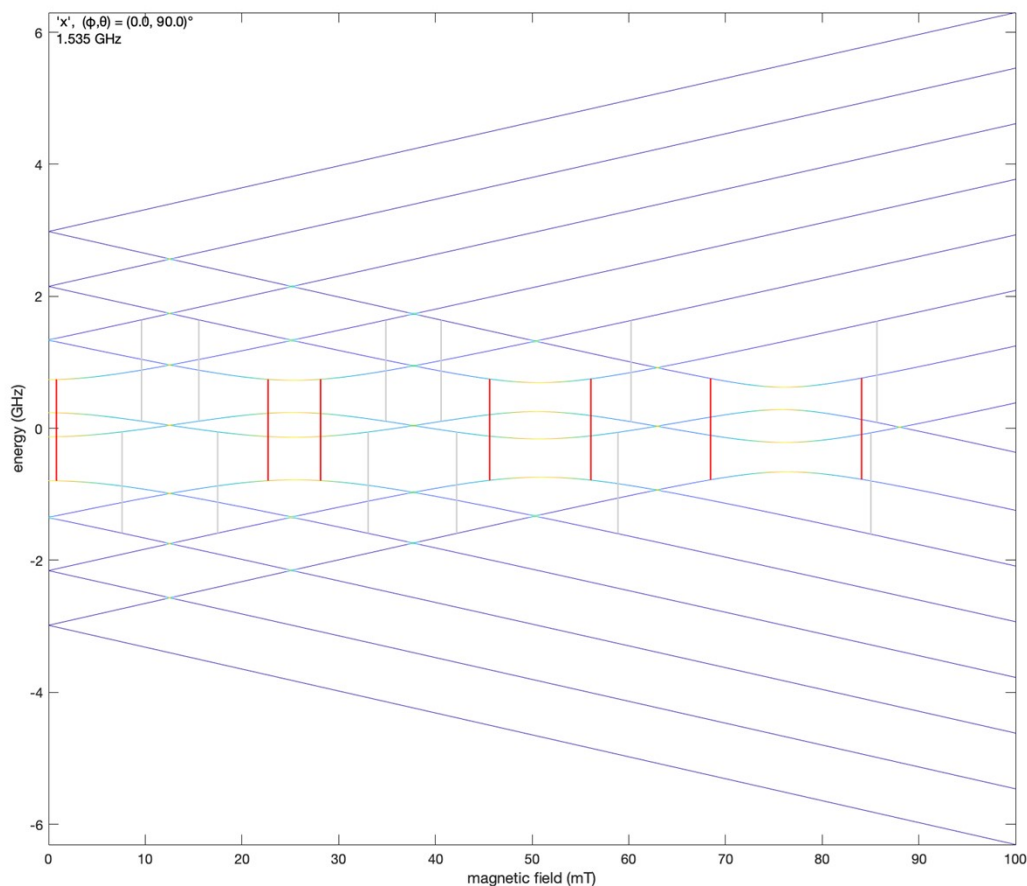


Figure S40. The energy level diagram of Co@Ni in the g_x direction based on the obtained EPR parameters at a closer look from 0 to 100 mT. Red bars indicate the resonance transitions at the microwave frequency of 1.535 GHz (in the L-band range).

Co(Hdmg)₂ synthesis and air oxidation

Figure S41 shows the attempt of the pure Co(Hdmg)₂ synthesis under air. When the reaction was carried out under air, the addition of the ligand to Co(II) solution immediately turned the solution dark brown, and no precipitate was observed. The removal of the MeOH solvent under reduced pressure by a rotary evaporator produced a sticky dark brown substance in Figure S41 c).

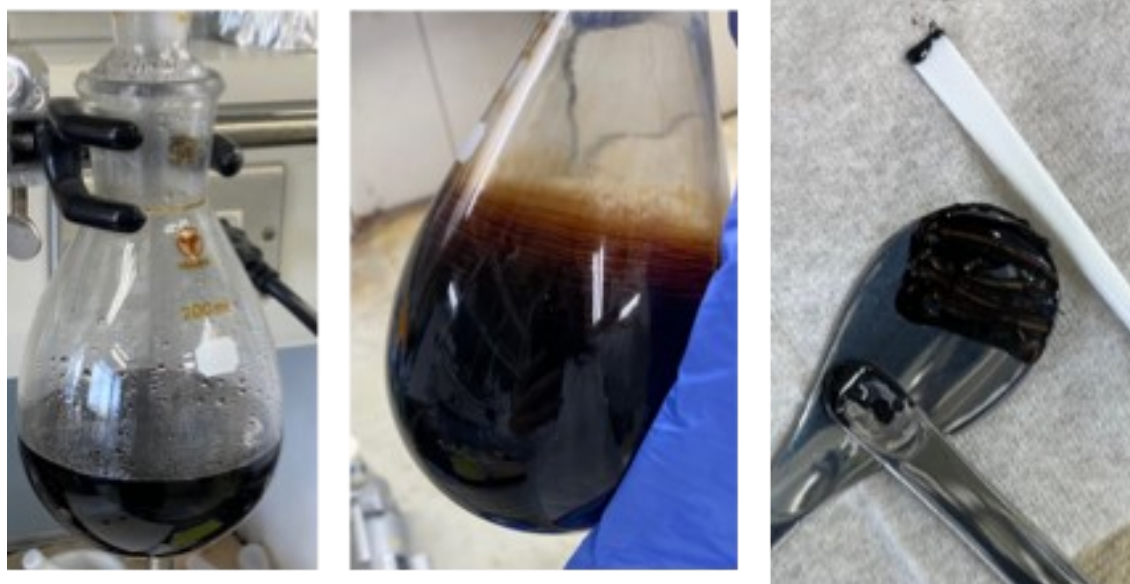


Figure S41. a) The reaction between $\text{Co}(\text{OAc})_2$ and the dimethylglyoxime ligand under air. No precipitate was observed under the air. b), c) after removing the solvent under vacuum. A sticky dark brown substance was obtained.

Figure S42 a) shows the reaction under the N_2 atmosphere. Dark orange precipitates were observed after the addition of the dimethylglyoxime ligand. When the mixture was brought into contact with air to collect the solid, the color of the mixture instantaneously turned into dark brown, and the dark orange precipitates turned into muddy blackish chunks in Figure S42 b).

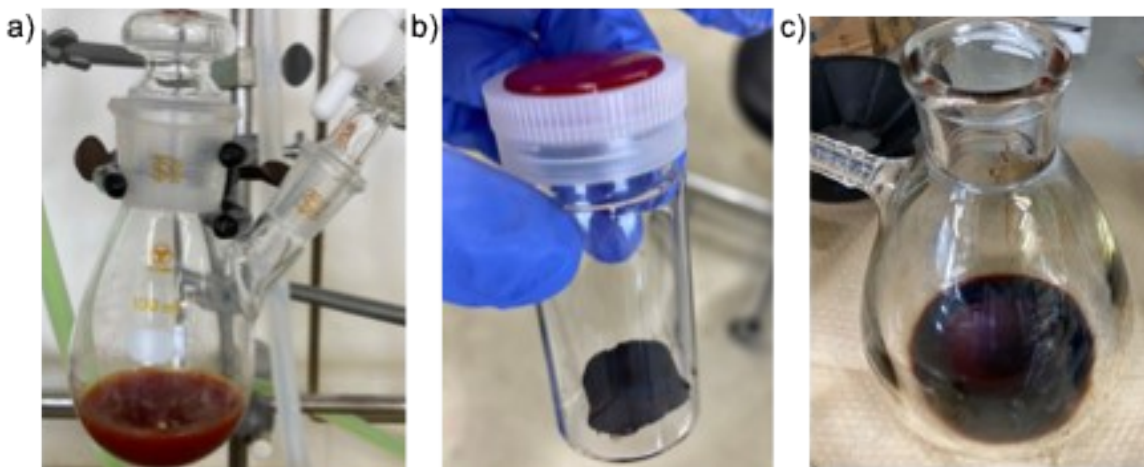


Figure S42. a) The reaction between $\text{Co}(\text{OAc})_2$ and the dimethylglyoxime ligand under N_2 atmosphere. The solution turned to orangish brown with precipitates. b). Filtered solid under air. Exposure to air turned the reaction mixture to dark brown immediately c) The filtrate under the air

IR Spectroscopy

The ATR-IR measurement of the pure $\text{Ni}(\text{Hdmg})_2$ and Co-doped $\text{Ni}(\text{Hdmg})_2$ gave almost identical results. No additional peak or noticeable difference was observed for the doped samples.

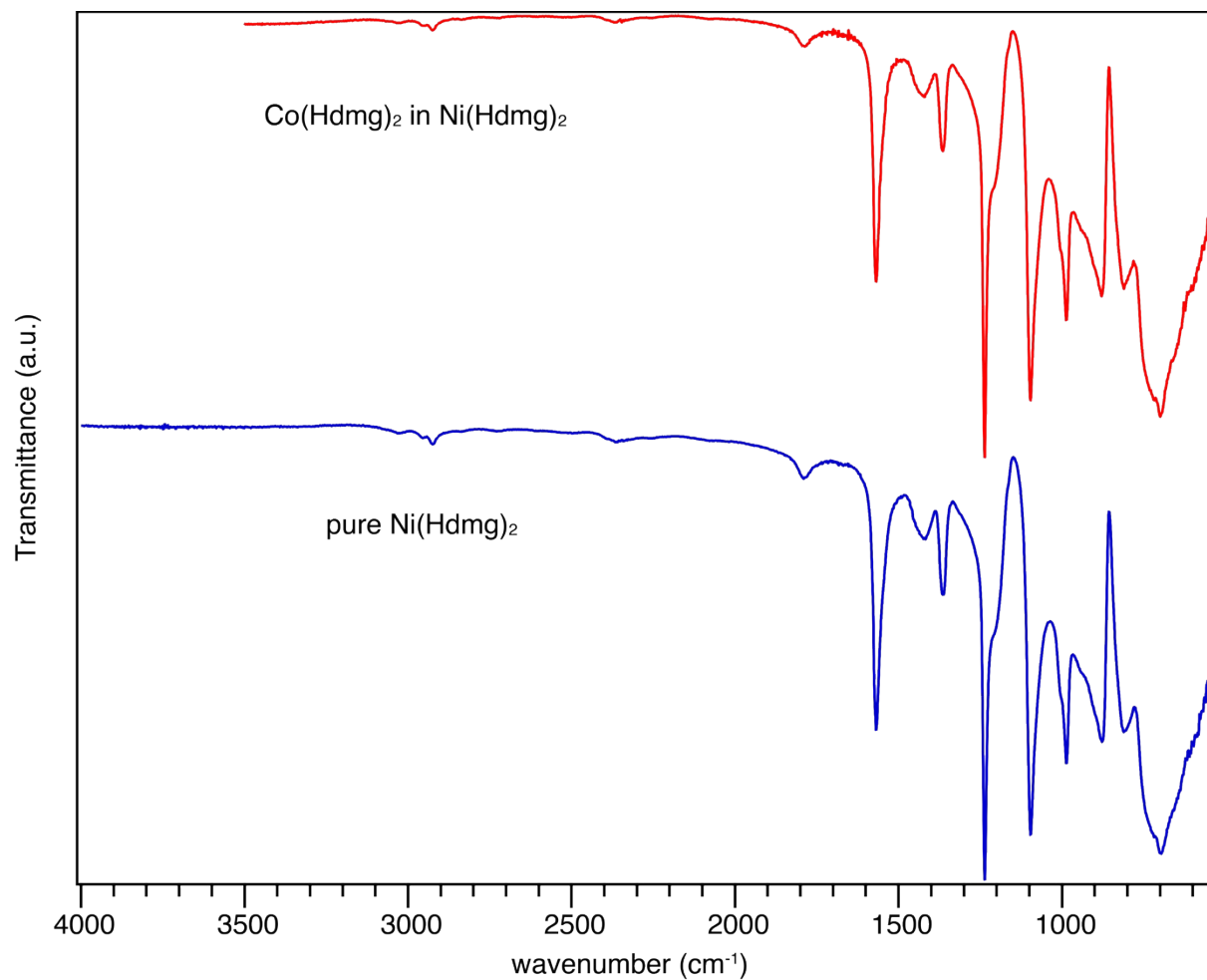


Figure S43. ATR-IR spectra of pure Ni(Hdmg)₂ and Co-doped Ni(Hdmg)₂

References

1. G. N. Schrauzer and R. J. Windgassen, *Chem. Berichte*, 1966, **99**, 602–610.
2. B. de Castro, M. Rangel and J. B. Raynor, *J. Chem. Soc., Dalton Trans.*, 1990, **0**, 3311–3318.
3. C. Floriani and F. Calderazzo, *J. Chem. Soc. A: Inorg., Phys., Theor.*, 1969, **0**, 946–953.
4. A. Dedieu, M. M. Rohmer and A. Veillard, *J. Am. Chem. Soc.*, 1976, **98**, 5789–5800.
5. J. P. Collman, R. R. Gagne, J. Kouba and H. Ljusberg-Wahren, *J. Am. Chem. Soc.*, 1974, **96**, 6800–6802.

6. W. Lubitz, C. J. Winscom, H. Diegruber and R. Mösele, *Z. für Naturforsch. A*, 1987, **42**, 970–986.
7. F. A. Walker, *J. Magn. Reson. (1969)*, 1974, **15**, 201–218.
8. M. Rangel, A. Leite, A. Silva, B. de Castro, W. Schlindwein and L. Murphy, *J Organomet Chem*, 2014, **760**, 11–18.
9. G. N. Schrauzer and L.-P. Lee, *J. Am. Chem. Soc.*, 1968, **90**, 6541–6543.
10. D. C. Lacy, G. M. Roberts and J. C. Peters, *J. Am. Chem. Soc.*, 2015, **137**, 4860–4864.
11. G. N. Schrauzer and L. P. Lee, *J. Am. Chem. Soc.*, 1970, **92**, 1551–1557.
12. M. Baumgarten, W. Lubitz and C. J. Winscom, *Chem. Phys. Lett.*, 1987, **133**, 102–108.
13. K. S. Min, J. Arthur, W. W. Shum, M. Bharathy, H.-C. zur Loye and J. S. Miller, *Inorg. Chem.*, 2009, **48**, 4593–4594.
14. K. Murray, A. Vandenberg, B. Kennedy and B. West, *Aust. J. Chem.*, 1986, **39**, 1479–1493.
15. J. Wan, Y.-F. Miao, X.-M. Li and S.-Sh. Zhang, *Asian Journal of Chemistry*, 2010, **18**, 1600–1606.
16. A. Rockenbauer, É. Budó-Záhonyi and L. I. Simándi, *J. Chem. Soc., Dalton Trans.*, 1975, **0**, 1729–1737.
17. T. Uruga, M. Tada, O. Sekizawa, Y. Takagi, T. Yokoyama and Y. Iwasawa, *Chem. Rec.*, 2019, **19**, 1444–1456.
18. B. Ravel and M. Newville, *J. Synchrotron Radiat.*, 2005, **12**, 537–541.
19. W. R. Hagen, *Int. J. Mol. Sci.*, 2023, **24**, 14793.
20. D. M. Jenkins, A. J. D. Bilio, M. J. Allen, T. A. Betley and J. C. Peters, *J. Am. Chem. Soc.*, 2002, **124**, 15336–15350.
21. Y. Journaux, O. Kahn, I. Morgenstern-Badarau, J. Galy, J. Jaud, A. Bencini and D. Gatteschi, *J. Am. Chem. Soc.*, 1985, **107**, 6305–6312.
22. S. Chandra, A. S. Hazari, Q. Song, D. Hunger, Nicolás. I. Neuman, J. van Slageren, E. Klemm and B. Sarkar, *ChemSusChem*, 2023, **16**, e202201146.
23. A. Bencini, C. Benelli, D. Gatteschi and C. Zanchini, *Proc. Indian Acad. Sci. - Chem. Sci.*, 1987, **98**, 13–22.

24. S. Grimme, *J. Comput. Chem.*, 2006, **27**, 1787–1799.
25. S. Grimme, J. Antony, S. Ehrlich and H. Krieg, *J. Chem. Phys.*, 2010, **132**, 154104.
26. M. Dolg, U. Wedig, H. Stoll and H. Preuss, *J. Chem. Phys.*, 1987, **86**, 866–872.
27. A. Bergner, M. Dolg, W. Küchle, H. Stoll and H. Preuß, *Mol. Phys.*, 1993, **80**, 1431–1441.
28. T. H. Dunning, *J. Chem. Phys.*, 1970, **53**, 2823–2833.
29. Thom. H. Dunning and P. J. Hay, 1977, 1–27.
30. D. Feller, *J. Comput. Chem.*, 1996, **17**, 1571–1586.
31. K. L. Schuchardt, B. T. Didier, T. Elsethagen, L. Sun, V. Gurumoorthi, J. Chase, J. Li and T. L. Windus, *J. Chem. Inf. Model.*, 2007, **47**, 1045–1052.
32. B. P. Pritchard, D. Altarawy, B. Didier, T. D. Gibson and T. L. Windus, *J. Chem. Inf. Model.*, 2019, **59**, 4814–4820.
33. M. J. Frisch, G. W. Trucks, H. B. Schlegel, G. E. Scuseria, M. A. Robb, J. R. Cheeseman, G. Scalmani, V. Barone, G. A. Petersson, H. Nakatsuji, X. Li, M. Caricato, A. V. Marenich, J. Bloino, B. G. Janesko, R. Gomperts, B. Mennucci, H. P. Hratchian, J. V. Ortiz, A. F. Izmaylov, J. L. Sonnenberg, Williams, F. Ding, F. Lipparini, F. Egidi, J. Goings, B. Peng, A. Petrone, T. Henderson, D. Ranasinghe, V. G. Zakrzewski, J. Gao, N. Rega, G. Zheng, W. Liang, M. Hada, M. Ehara, K. Toyota, R. Fukuda, J. Hasegawa, M. Ishida, T. Nakajima, Y. Honda, O. Kitao, H. Nakai, T. Vreven, K. Throssell, J. A. M. Jr., J. E. Peralta, F. Ogliaro, M. J. Bearpark, J. J. Heyd, E. N. Brothers, K. N. Kudin, V. N. Staroverov, T. A. Keith, R. Kobayashi, J. Normand, K. Raghavachari, A. P. Rendell, J. C. Burant, S. S. Iyengar, J. Tomasi, M. Cossi, J. M. Millam, M. Klene, C. Adamo, R. Cammi, J. W. Ochterski, R. L. Martin, K. Morokuma, O. Farkas, J. B. Foresman and D. J. Fox, *Gaussian 16 Rev. C.01*, Wallingford, CT, 2016.
34. F. Neese, *Wiley Interdiscip. Rev.: Comput. Mol. Sci.*, 2012, **2**, 73–78.
35. F. Neese, *Wiley Interdiscip. Rev.: Comput. Mol. Sci.*, DOI:10.1002/wcms.1606.
36. J. P. Perdew, *Phys. Rev. B*, 1986, **33**, 8822–8824.
37. A. D. Becke, *Phys. Rev. A*, 1988, **38**, 3098–3100.
38. F. Neese and E. I. Solomon, *Inorg. Chem.*, 1998, **37**, 6568–6582.
39. F. Neese, *J. Am. Chem. Soc.*, 2006, **128**, 10213–10222.
40. F. Neese, T. Petrenko, D. Ganyushin and G. Olbrich, *Coord. Chem. Rev.*, 2007, **251**, 288–327.

41. M. Atanasov, D. Aravena, E. Suturina, E. Bill, D. Maganas and F. Neese, 2015, **289–290**, 177–214.
42. I. Malkin, O. L. Malkina, V. G. Malkin and M. Kaupp, *Chem. Phys. Lett.*, 2004, **396**, 268–276.
43. F. Weigend and R. Ahlrichs, *Phys. Chem. Chem. Phys.*, 2005, **7**, 3297–3305.
44. F. Neese, F. Wennmohs, A. Hansen and U. Becker, *Chem. Phys.*, 2009, **356**, 98–109.
45. A. Kumar, R. P. Tandon and V. P. S. Awana, *J. Appl. Phys.*, 2011, **110**, 043926.
46. J. A. Mydosh, *CRC Press.*, DOI:10.1201/9781482295191.
47. G. Eiselt, J. Kötzler, H. Maletta, D. Stauffer and K. Binder, *Phys. Rev. B*, 1979, **19**, 2664–2676.
48. L. W. Bernardi, H. Yoshino, K. Hukushima, H. Takayama, A. Tobo and A. Ito, *Phys. Rev. Lett.*, 2001, **86**, 720–723.
49. G. Hu, J. Xia and Q. Yang, *J. Alloy. Compd.*, 2024, **1008**, 176562.
50. H. Akamatsu, K. Tanaka, K. Fujita and S. Murai, *Phys. Rev. B*, 2006, **74**, 012411.
51. M. Kofu, R. Watanuki, T. Sakakibara, S. Ohira-Kawamura, K. Nakajima, M. Matsuura, T. Ueki, K. Akutsu and O. Yamamuro, *Sci. Rep.*, 2021, **11**, 12098.
52. A. K. Bhatti, N. Jabeen, A. Bashir, L. U. Khan, S. W. Bokhari and Z. Akhter, *RSC Adv.*, 2023, **13**, 28602–28612.
53. B. Yildirim and H. Riesen, *J. Phys.: Conf. Ser.*, 2013, **430**, 012011.
54. J. A. BEARDEN and A. F. BURR, *Rev. Mod. Phys.*, 1967, **39**, 125–142.
55. M. Giorgetti, S. D. Longa and M. Benfatto, *J. Phys.: Conf. Ser.*, 2009, **190**, 012145.
56. Y. Liu, A. Deb, K. Y. Leung, W. Nie, W. S. Dean, J. E. Penner-Hahn and C. C. L. McCrory, *Dalton Trans.*, 2020, **49**, 16329–16339.
57. C. Johnson, B. Long, J. G. Nguyen, V. W. Day, A. S. Borovik, B. Subramaniam and J. Guzman, *J. Phys. Chem. C*, 2008, **112**, 12272–12281.